Layer-by-Layer Assembly of CTAB-rGO-Modified MXene Hybrid Films as Multifunctional Electrodes for Hydrogen Evolution and Oxygen Evolution

ACS OMEGA

Open Access

http://pubs.acs.org/journal/acsodf

Article

Layer-by-Layer Assembly of CTAB-rGO-Modified MXene Hybrid Films as Multifunctional Electrodes for Hydrogen Evolution and Oxygen Evolution Reactions, Supercapacitors, and DMFC Applications

Asha Raveendran, Mijun Chandran, Masoom Raza Siddiqui, Saikh Mohammad Wabaidur, Muthusankar Eswaran, and Ragupathy Dhanusuraman*

Cite This: *ACS Omega* 2023, 8, 34768−34786

Read Online

ACCESS | Metrics & More | Article Recommendations | Supporting Information

ABSTRACT: Exceptional electrical conductivity and abundance of surface terminations like−F− and OH− leading to hydrophilicity make the family of 2D transition metal carbides/nitrides and carbonitrides (MXene) excellent candidates for energy storage and conversion applications. MXenes, however, undergo restacking of nanosheets via van der Waals interaction, hindering the active sites, leading to slow electronic and ionic kinetics, and ultimately affecting their electrochemical performance. Herein, we report binder-free cetyltrimethylammonium bromide-reduced graphene oxide (CTAB-rGO)-modified MXene hybrid films on nickel foam as a promising noble metal-free multifunctional electrode synthesized via layer-by-layer assembly and dip coating techniques, which effectively reduce restacking while improving the kinetics. The properties of the as-prepared electrocatalysts are investigated using various physiochemical characterizations and electrochemical measurements to accomplish the objective of "creating one kind of electrocatalyst for multiapplication" with a thorough understanding of the relationship between the material structure, morphology, and electrocatalytic performance. In energy conversion, the synergetic effect of MXene and the CTAB-rGO support helped increase the catalytic activity of the composite for electrochemical water splitting, demonstrating a current density of 10 mA/cm^2 at an overpotential (η) of 360 V and a Tafel slope value of 56.6 mV/dec for hydrogen evolution reaction and a current density of 10 mA/cm^2 at an overpotential (η) of 179 mV and a Tafel slope value of 47.03 mV/dec for oxygen evolution reaction in an alkaline medium. The electrode material also exhibited a higher oxidation current density (373.60 mA/cm^2) compared to that of synthesized MXene toward methanol oxidation reaction in direct methanol fuel cell application. Additionally, the energy storage potential of CTAB-rGO modified MXene as electrode materials for supercapacitors with a high specific capacitance (544.50 F g^{-1} at 0.5 A g^{-1}) and a good capacity retention of 87% after 5000 cycles was studied. These findings of this work showcase the potential of the electrocatalyst in both conversion and storage of electrochemical energy.

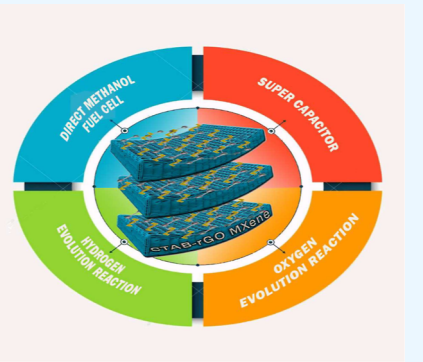

1. INTRODUCTION

The world's current energy crisis is caused by the never-ceasing depletion of the oil resources and the deterioration of the ecological environment primarily due to carbon dioxide-emitting fossil fuels and has encouraged scientists to research green energy and renewable sources.[1−6] Numerous businesses have shifted focus on the automotive market to lessen the world's reliance on petroleum resources, including big names like Honda, Mercedes-Benz, Hyundai, and Tesla, to emphasize the usage of hybrid materials for fuel cells and electric motors using green energy.[7,8] Issues concerning global warming, pollution, and a suitable energy alternative that could replace non-renewable energy and equip the ever-growing population have resulted in more attention being placed on electrochemical energy applications like supercapacitors,[9−11] fuel cells,[12,13] and electrochemical water splitting,[14,15] thanks to their environmental friendliness, good cyclic stability, and high power density. The high power density of the supercapacitors and the minimal operating temperatures of the fuel cells like the proton exchange membrane fuel cells,[16] alkaline electrolyzers, and direct methanol fuel cells (DMFCs) could effectively produce clean and green energy.[17] They have been prioritized as critical for future energy storage and conversion technologies. However, the bottleneck issues of the electrochemical reactions of these applications include (a) methanol oxidation reaction (MOR):[18] slow kinetics and intermediates like carbon monoxide (CO) easily poison the anodic electrocatalyst and

Received: May 31, 2023
Accepted: August 31, 2023
Published: September 14, 2023

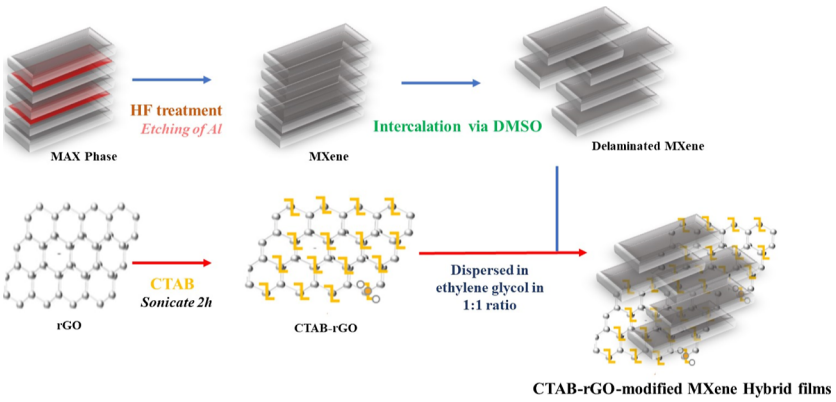

Figure 1. synthesis of CrMX is depicted in a schematic form.

worsen the DMFC performance, (b) electrocatalytic water splitting:[19] both hydrogen and oxygen evolution reactions (HER and OER) involve multiple electron transport, and OER also includes breaking and formation of the O−H and O−O bonds, all of which require a high overpotential, and (c) supercapacitors:[20] inadequate energy density caused by the supercapacitor electrode's poor ionic and electronic conductivity, all of which need to be addressed.[21] Among the promising candidates of green energy storage devices, supercapacitors are widely adopted due to their rapid charge−discharge abilities, higher power density, and long cyclic stability, which would, for any practical application, allow electronic devices to be continuously used for an extended period and to be fully charged in a short duration.[22−25] However, developing an electrode material that is fast charging−slow discharging with an excellent performance rate is still challenging. When it comes to the need of green fuel for energy conversion, the usage of renewable energy sources like hydrogen is also thought to hold great promise for resolving the environmental problems, and one of the most cleanest methods of energy conversion currently being used is hydrogen generation via HER, i.e., via water electrolysis converting electrical energy into hydrogen energy.[26−28] Besides the electrolysis of water for hydrogen fuel, due to better efficiency and low emission levels, DMFCs have also been acknowledged as promising energy sources for mobile electronics and automobiles.[29−31] Compared to the hydrogen fuel cells, DMFCs have a higher energy density and exhibit easier solubilization of raw materials. However, the commercialization of these fuel cells has been constrained by high manufacturing costs, slowly occurring oxidation reaction of methanol on the anode of the fuel cell, and the production of carbon dioxide during their oxidation.[32−34] Hydrogen, on the other hand, is a zero-emission greenhouse gas and is hence wholly green.[35,36]

In order to achieve optimal performance for supercapacitors, electrochemical water splitting, and fuel cells, in conventional globalized electrochemical applications, platinum (Pt), gold (Au), ruthenium (Ru), palladium (Pd), and other noble metal electrodes[37,38] are used and are considered state-of-the-art electrode materials for the fuel cells. These noble metals when accompanied with a carbon-based supercapacitor electrode were observed to exhibit a much better capacitance and improved stability.[39,40] However, they are scarce and are highly expensive.[41−43] Development of earth-abundant materials with low activation energy and high capacitance that allow for efficient energy conversion and storage represents a significant obstacle to the implementation of these green energy systems.[44,45] Furthermore, producing an electrode material capable of both energy storage and conversion could reduce the expenses and make integration convenient.

Transition metal nitrides and carbides/carbonitrides collectively called MXenes are a promising and evolving family of 2-dimensional nanosheets, first synthesized by Gogotsi and group in 2011. The general composition is $M_{n+1}X_nT_x$, (n = 1, 2, 3), where M denotes an early transition metal, X is C and/or N, and T_x signifies the surface functional groups (−O,−OH and/or −F). MXenes are synthesized from the ternary layered MAX phase by selectively extracting the "A" layers, where A is group IIIA/IVA elements.[46,47] Their metallic conductivity, 2D layered structure, mechanical stability, good hydrophilicity, and surface chemistry have drawn attention toward MXene for application in fuel cells like DMFCs, Li-ion batteries, electrochemical water splitting, biosensors, and energy storage devices like supercapacitors.[48−50] The hydrophilic nature due to the surface terminations, the transition metals attributing to the metallic nature and various electronic states, and layered structure which enhances the surface area make MXene ideal electrocatalysts for overall water splitting.[51,52] The HER performance of Ti-MXene was evaluated by Jiang and group where the oxygen-rich termination improved the proton adsorption and displayed a Tafel slope of 60.7 mV/dec with a low overpotential at 10 mA cm^{-2}.[53] NiCuS@Ti-MXene synthesized by Zou et al. showed a Tafel slope of 58.2 mV/dec at an overpotential of 365 mV @ 10 mA cm^{-2} for OER.[54] In supercapacitors, they are more promising than the traditional carbon-based electric double-layer capacitors (EDLCs) as they exhibit better density and greater psuedocapacitance.[55,56] The durable van der Waals attraction among the adjacent MXene nanosheets leads to their self-restacking and aggregation, thereby causing a drastic loss of catalytically active sites for electrocatalysis and limiting the transportation of ions. Strategies such as introducing spacers such as 3-dimensional macroscopic structures and 2-dimensional nanosheets are considered in order to completely utilize the electrochemical performance.[57,58] Graphene oxide (GO) is another 2-dimensional material, which exhibits good porosity, extensive surface area, and tremendous mechanical and chemical stability. GO has a high degree of defects and a disruption in the network of sp^2-bonding of the carbon atoms. To restore graphene's π network, GO should be reduced, yielding reduced GO (rGO). The presence of the defective sites even after reduction gives rGO the ability to decorate with a variety of functional groups.[59,60] Thus, owing to the intrinsic accordion-like structure, $Ti_3C_2T_x$ combines with rGO via self-assembly, thus not only preventing the restacking of MXene nanosheets

https://doi.org/10.1021/acsomega.3c03827
ACS Omega 2023, 8, 34768−34786

but also quickening the charge transfer across various nanosheets' interfaces.[61]

The common technique for preparing the electrodes for the study of electrocatalysis and supercapacitor behavior mentioned earlier is to combine the active material, binder, and conductive materials like activated charcoal in the right proportions. The mixture is then ground and applied to a current collector (such as nickel foam) surface. Grinding could damage the active material's structure, and the binder also raises the electrode resistance. In this work, the authors showcase the fabrication of binder-free $Ti_3C_2T_x$ (MXene) and rGO hybrid film electrode material (CrMX) using the layer-by-layer assembly of reduced GO positively charged via surfactant cetyltrimethylammonium chloride (CTAB) and negatively charged $Ti_3C_2T_x$. The substrate material used here was a nickel foam, and the electrocatalyst was adhered onto the support via dip coating; its electrochemical activity toward electrochemical water splitting (which includes both OER and HER), supercapacitor, and DMFC was analyzed. The synthesis of CrMX is depicted in a schematic form in Figure 1. The resulting electrode material possesses several advantages: the layered 2-dimensional structures and the porous framework allow the diffusion of the electrolyte within the interface and also provide abundant electroactive sites, and the CTAB-rGO and MXene networks enhance rapid hydrogen evolution, oxygen evolution, and methanol evolution kinetics owing to their low charge resistance. As a result, the synthesized noble metal-free catalyst expressed good cyclic stability, faster charge−discharge, and better catalytic activity for energy storage and conversion applications.

2. EXPERIMENTAL METHOD

2.1. Materials. Ti_3AlC_2 (MAX Phase) and rGO were procured from Sigma-Aldrich. Dimethyl sulfoxide (DMSO) (>99.7%) and CTAB were from Fischer Scientific. Hydrofluoric acid (40%), methanol (99%), and ethylene glycol (99%) were purchased from Nice. Potassium hydroxide [ACS reagent, ≥85%, pellets] was purchased from Merck Chemicals. Milli-Q water was used to prepare all the aqueous solutions.

2.2. Synthesis of Delaminated MXene from Precursor MAX Phase. For the purpose of selectively etching the Al-layer from Ti_3AlC_2, approximately 3 g of precursor Ti_3AlC_2 was added to 40 mL of hydrofluoric acid (40%) gradually and stirred continuously for 96 h. To neutralize the pH, the powder obtained was centrifuged and then washed. $Ti_3C_2T_x$ (MXene), the resulting residue, was dried at 75 °C overnight. MXene was delaminated by dispersing the synthesized material into 50 mL of DMSO solution and then stirring continuously at room temperature for 24 h. The aforementioned solution was twice rinsed with deionized water before being centrifuged for 10 min at 3500 rpm. This is followed by decantation and then sonication with deionized water. The delaminated MXene layers were separated from the supernatant solution.

2.3. Synthesis of CrMX (CTAB-rGO with MXene). 100 mL of aqueous solution of CTAB (2 mg/mL) and 100 mL of aqueous solution of rGO (1 mg/mL) were vigorously sonicated for 2 h before being rinsed with deionized water till the pH reached a value around neutral (7). At 50 °C, the mixture was dried for 6 h. 20 mL of aqueous $Ti_3C_2T_x$ (1 mg/mL) was combined with CTAB-rGO in an ethylene glycol dispersion in the ratio of 1:1.

2.4. Fabrication of the Electrode Material. Using a dip-coating technique, the negatively charged MXene sheets due to the O− and F− terminations and the rGO sheets which are positively charged by the surfactant CTAB (CrMX) were deposited on a commercial nickel foam (measuring 2 cm × 1 cm, 1.6 mm in thickness). First, the nickel foam was cleaned by treating it with 3 M HCl for 30 min, followed by treatment with acetone via ultrasonication. After thorough cleaning, the nickel foam was dried for 2 h at 60 °C in a vacuum oven. After being cleaned, the nickel foams were dipped in the CrMX suspension (2 mg/mL) for 10 s, removed, and dried for 30 min in a vacuum oven at 80 °C. To form an interconnected conduction network and achieve the lowest resistances, the dip coating of $Ti_3C_2T_x$ with the CTAB-rGO sheets (CrMX) are sufficient after the fifth dipping−drying cycle. Repetitive stacking in the pores of the Ni foam would result from further extending the number of dip-coating cycles. Dip coating of MXene and rGO on the nickel foam was carried out using the above-mentioned techniques using the MXene and rGO suspensions. Notably, the nickel foam's immersion area measured 1 × 1 cm^2 for each sample, and the samples were dried vertically. Weighing the nickel foam prior to and following coating allowed us to calculate the mass loading and was found to be 2 mg cm^{-2}.

2.5. Material Characterizations. Scanning electron microscopy (SEM) images were used for investigating the morphology, and the elemental distribution with the elemental mapping of the electrode materials was determined using a JCM-7000 NeoScope Benchtop. The crystalline structure of the manufactured electrodes was investigated using X-ray diffraction (XRD) analysis using a PANalytical X'Pert PRO equipped with an X'Celerator position sensitive detector and Cu K radiation of wavelength = 1.5401. Using the Fourier transform infrared (FTIR) spectrometer, PerkinElmer spectrum 2, FTIR spectroscopy was performed to examine the functional groups of the electrodes in the wavenumber region between 4000 and 400 cm^{-1}. The Brunauer−Emmett−Teller (BET) method was used to compute the textural and the pore properties of the materials using an Anton Paar Nova 800. The materials' X-ray photoelectron spectra (XPS) were captured using a Thermo Fisher Scientific (Model K-Alpha) instrument. The Metroohm (Multi Auto lab/M204) [Switzerland] electrochemical work station was used to test the electrochemical performance of the electrodeposited electrodes.

2.6. Electrochemical Measurements. The electrocatalytic measurements were performed at room temperature via Metroohm (Multi Auto lab/M204) using a three-electrode system. The prepared electrodes, a silver, silver chloride electrode, and a platinum rod were utilized as working electrodes, reference electrodes, and counter electrodes, respectively. The synthesized electrocatalysts were coated onto the substrate electrode, the nickel foam, through the layer-by-layer assembly method and the dip-coating method. The supercapacitor characteristics and OER, HER, and methanol oxidation performances were evaluated in the alkaline medium of 1.0 M KOH after being thoroughly deaerated by high-purity nitrogen. CTAB-rGO-modified MXene was utilized both as a cathode and an anode for testing electrochemical water splitting using a two-electrode system. Based on the Nernst equation, the potential versus reversible hydrogen electrode (RHE) was calculated using the equation

$$E_{RHE} = E_{Ag/AgCl} + 0.059pH + E^{o}_{Ag/AgCl} \quad (1)$$

At a scan rate of 5 mV/s, the linear sweep voltammetry (LSV) was tested, and the linear sweep curves were *iR*-corrected. The equations represent how *IR* compensation is expressed.

https://doi.org/10.1021/acsomega.3c03827
ACS Omega 2023, 8, 34768−34786

$$E_{\text{correction}} = I \times R$$

$$E_{\text{corrected}} = E_{\text{uncorrected}} - E_{\text{correction}} = E_{\text{uncorrected}} - I \times R$$

where I is the measured current, R is the uncompensated resistance as determined from electrochemical impedance spectra (EIS), and E is the measured potential with regard to RHE.

The Tafel slopes, overpotential, and exchange current density were calculated. Using simple cyclic voltammetry (CV), electrochemically active surface area (ECSA) was acquired by varying the scan rates based on the double-layer capacitance (C_{dl}). The long-term durability of the electrodes was tested by chronoamperometry measurements in 1.0 M KOH. The specific capacitances were calculated from the cyclic voltammograms and galvanostatic charge/discharge curves. Power and energy density were also calculated and compared with those from other works in the Ragone plot. The charge-transfer resistances and kinetics of the electrodes are derived from EIS. The ability of CrMX to electrooxidize methanol is also tested by conducting cyclic voltammetric studies in the presence of methanol.

3. RESULTS AND DISCUSSION

3.1. Physiochemical Characterization. The XRD patterns of Ti_3AlC_2 used as a precursor for the etched $Ti_3C_2T_x$ in the hydrofluoric acid along with rGO and the final composite, and CTAB-rGO-modified MXene are shown in Figure 2. Strong

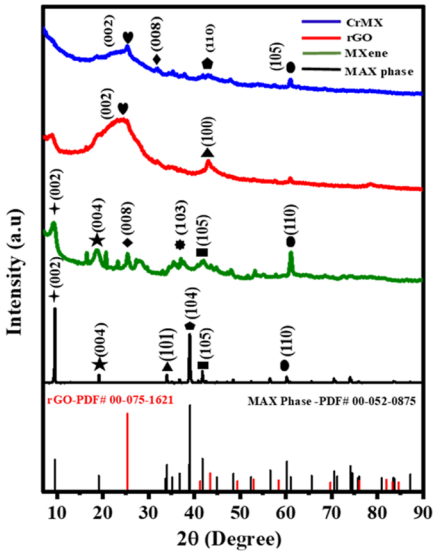

Figure 2. XRD patterns of MXene, MAX phase (Ti_3AlC_2), rGO, and CrMX.

diffraction peaks of Ti_3AlC_2 MAX phase at angle 2θ = 9.3,19.4, 34.1, 39, 41.6, 48.3, 60.3, 70.6, and 74.5° corresponding to the (002), (004), (101), (104), (105), (110), (118), and (1013) planes, respectively, are in accordance with the ICDD card number 52-0875. Indicating MXene's bigger d spacing following the etching of the aluminum layer, the peak of the (002) and (004) planes at 9.3 and 19.4°, respectively, of Ti_3AlC_2 shifted to lower 2θ values following treatment with HF. According to the XRD patterns of MXene and MAX phase, the sharpest non-basal plane peaks around 38.9° of the precursor are absent in $Ti_3C_2T_x$. Additionally, the peaks of the planes (002) and (004) appear to be shifted to lower angles and broadened with less intensity, in comparison to their positions prior to treatment, which denote the etching of aluminum and MXene formation. The peaks at 35.4 and 41.3° correspond to the (103) and (105) planes, respectively, which indicate the presence of the TiC impurity, and the peak at 27.7° (008) confirms the formation of $Ti_3C_2(OH)_2$. The broad peaks at 2θ = 24.6 and 42.5° for rGO are the diffraction patterns of the crystallographic planes (002) and (100), respectively, related to the presence of the accumulated graphene sheets and a hexagonal carbon structure in accordance to the ICDD card number 75-1621. However, because of the nanostructured rGO formation linked to MXene, the MXene peaks like those of (002) and (100) were hidden in the CrMX patterns; besides, the diffraction patterns of both MXene and rGO are seen in the XRD patterns of CrMX.

The surface morphology of CrMX and MXene is provided in Figures 3 and S1c,d, while the MAX phase and rGO are depicted in Figure S1. The SEM images of MXene exhibit an accordion-like structure and those of CrMX demonstrate the intercalation of rGO within the layers of MXene, concealing the structures that resemble the accordions of MXene, giving a three-dimensional appearance. The interconnected network system avails numerous ion intercalation sites, ensuring faster electron transfer and ion diffusion along with volume expansion. Energy-dispersive X-ray spectroscopy (EDX) of $Ti_3C_2T_x$ MXene reveals that Ti, O, C, and F are all evenly distributed, and CrMX depicts a greater percentage of carbon along with Ti, O, and F, which further confirms the successful incorporation of rGO within MXene. Elemental mapping of MXene and rGO is provided in the Supporting Information (Figures S2 and S3).

Figure 4a−c displays the TEM images and the elemental mapping of CrMX. The TEM images illustrate MXene and rGO's interconnected sheet-on-sheet networks, which ensures quick ion diffusion and electron transfer. The nanosheet assembly can be seen in these images, which also demonstrate the minimal self-restacking of the MXene nanosheets. The absence of significant wrinkles in MXene, in contrast to rGO, suggests that as compared to rGO, the MXene sheets are less flexible. Parallel fringes with lattice spacings of 0.576 and 0.375 nm are visible in the corresponding high-resolution TEM image corresponding to the (002) plane of rGO and the (004) plane of MXene (Figure 4c), proving that $Ti_3C_2T_x$ MXene and rGO are coexisting. Ti, O, C, and F are evenly distributed on a large scale according to the elemental mapping of CrMX. Thus, the interconnected sheet-on-sheet network formation between MXene and rGO along with the SAED pattern from the TEM analysis and the intercalation of rGO within the MXene layers as observed in SEM images give validation of the successful synthesis of CrMX.

The pore size distributions and N_2 adsorption and desorption isotherms of CrMX and MXene are shown in Figures 5 and S5, respectively. The isotherm has both MXene and CrMX , which are mesoporous in nature. The surface areas of CrMX and MXene are 21.437 and 15.50 m^2/g, respectively. The successful incorporation of rGO within the MXene layers may account for the improved surface area of CrMX over that of MXene. CrMX and MXene have pore volumes of 0.0421 & 0.025 cm^3/g, respectively, of which CrMX's average pore diameter was found to be 7.8613 nm.

The surface conditions of CrMX, MXene, and rGO were observed by FTIR studies in Figure 6. In MXene, the dip at 3132 cm^{-1} corresponds to the hydroxyl group, and those at 2368.5 and 2067.7 cm^{-1} correspond to the hydrogen bond owing to the presence of the oxygenated groups. The dip at 1720.5 cm^{-1} corresponds to the C═O bonding, while that at 1396.5 cm^{-1} is

https://doi.org/10.1021/acsomega.3c03827
ACS Omega 2023, 8, 34768−34786

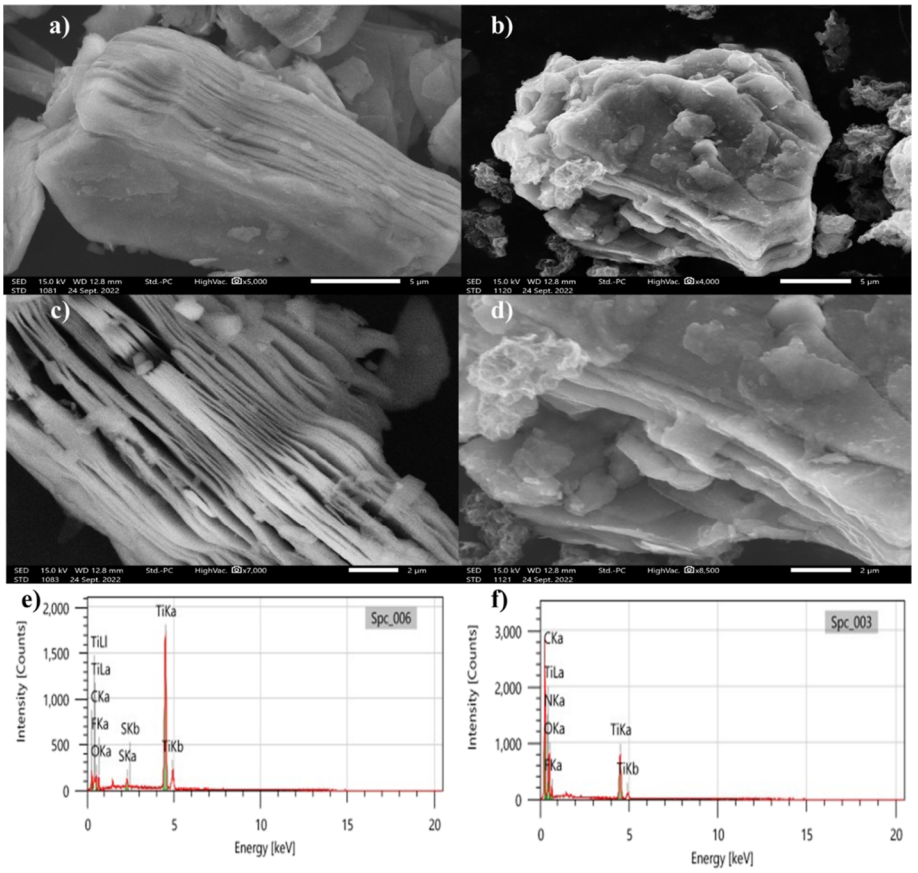

Figure 3. SEM images of (a,c) MXene and (b,d) CrMX and EDX spectra of (e) MXene and (f) CrMX.

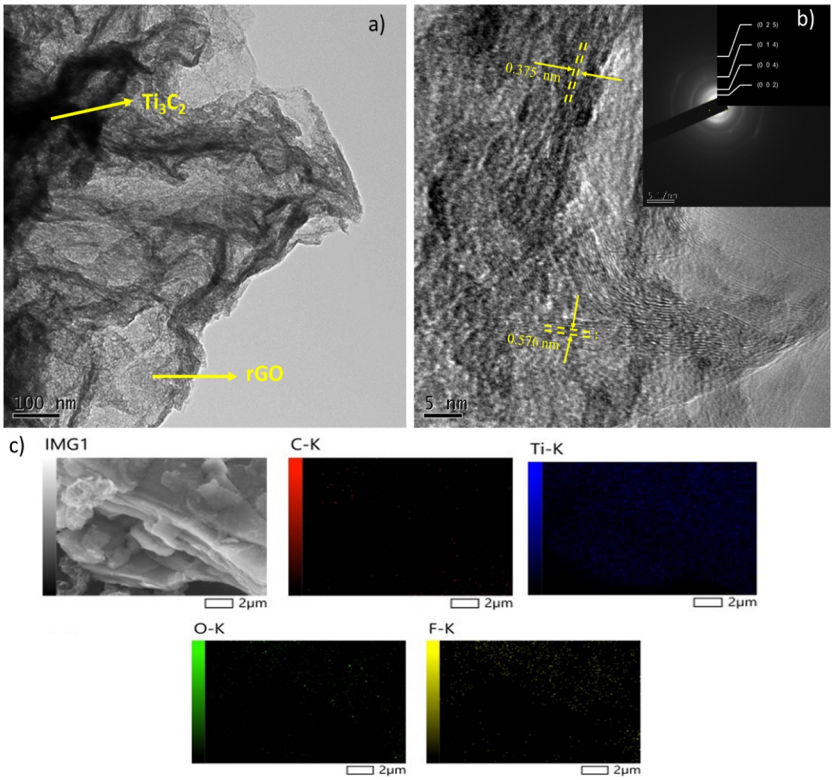

Figure 4. TEM images of (a,b) CrMX with the inset containing the SAED pattern and (c) elemental mapping of CrMX.

https://doi.org/10.1021/acsomega.3c03827
ACS Omega 2023, 8, 34768−34786

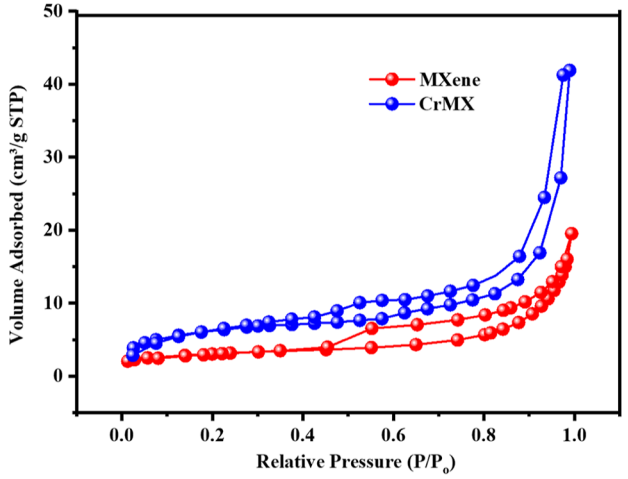

Figure 5. N_2 adsorption/desorption isotherm of CrMX and MXen.

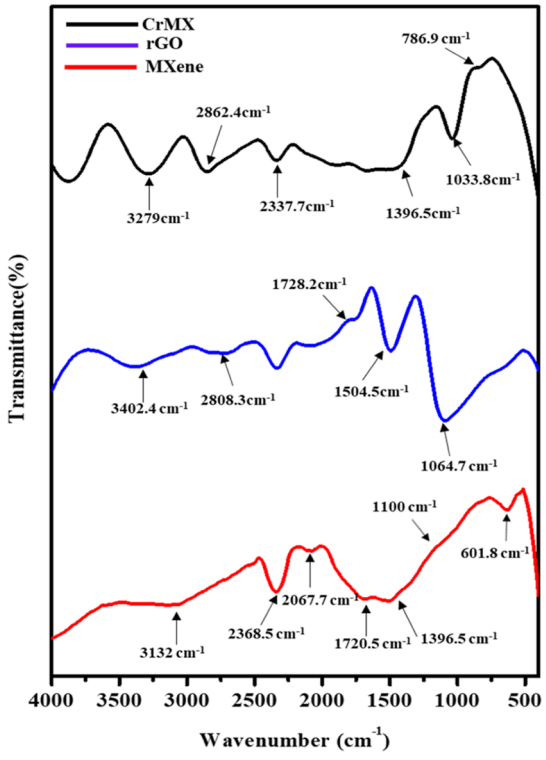

Figure 6. FTIR analysis of MXene, rGO, and CrMX.

due to molecular water (O−H), and the absorbance peaks at 1100 and 601.8 cm^{-1} belong to the C−F vibration and deformation vibration of the Ti−O bond, respectively. The absorption peaks observed in the FTIR spectra of rGO observed at 3402.4, 2808.3, 1728.3, 1504.5, and 1064.7 cm^{-1} belong to the O−H stretching vibration, symmetric C−H stretching vibration, C═O stretching vibration, C−C stretching vibration, and C−O stretching vibration, respectively. In CrMX, peaks of both MXene as well as rGO are observed, and the peak at 786.9 cm^{-1} confirms the formation of the Ti−O−C bonding.

The CrMX elemental composition and surface electronic states are further revealed by XPS. According to the XPS survey spectrum in Figure S4a Supporting Information, the CrMX nanocomposite is primarily made up of the elements C, Ti, O, and F, with the elements C and O originating from both rGO and MXene and the elements Ti and F originating from MXene. Figure 7a displays the Ti 2p XPS spectra of CrMX, where the equivalent spectrum is fitted with six peaks. Ti(II) $2p_{3/2}$ and Ti(II) $2p_{1/2}$ correspond to 459.78 and 462.35 eV, Ti(III) $2p_{3/2}$ and Ti (III) $2p_{1/2}$ correspond to 459.68 and 464.88 eV, and C−Ti−F and $TiO_{2-x}F_X$ correspond to 465.68 and 467.48 eV, respectively. Figure 7b shows the C 1s XPS spectra fitted with six peaks of 284.68, 285.58, 287.08, 287.28, 289.08, and 289.13 eV that correspond to Ti−C−O, C−C, C−O, CH_x, C═O, and C−F, respectively. As depicted in the O 1s XPS spectrum in Figure S4b, the fitted peaks at 530.98, 532.28, and 533.88 eV are attributed to C−Ti−O_x, C−Ti−OH_x, and C═O, respectively. Figure S4c depicts the F 1s region of the CrMX high-resolution XPS spectra. It demonstrates that the F 1s region was primarily composed of 685.28, 686.28, and 690.08 eV, which corresponded to the C−Ti−F, F contamination, and $Al(OF)_x$, respectively.

3.2. Electrochemical Characterization. *3.2.1. Electrochemical HER.* The electrocatalytic activity of CTAB-rGO-modified MXene (CrMX) is compared with those of pristine MXene and rGO for their HER activity, which was studied by analyzing the polarization plots in N_2-saturated 1 M KOH. With reference to the potentials of the Ag/AgCl electrode, LSV measurements for HER were carried out; eq 1 was then used to convert these potentials into RHE scale. The polarization curves of the three electrocatalysts in Figure 8a allow for a comparison at 5 mV/s scan rate where the HER electrocatalytic activity of the CrMX was found to be better than those of MXene and rGO. Electrochemical impedance measurements were used to validate the electrochemical performance of the synthesized electrocatalysts and to study the uncompensated resistance. The Tafel slopes are derived from the Tafel plots after *iR* compensation for all the three electrocatalysts and are summarized along with the exchange current density and overpotential in Table 1.

To derive the Tafel slope, the Tafel equation was used in the form of

$$\eta = b \log j + a \tag{2}$$

where η is the overpotential of the electrode, j is the current density, a is the Tafel intercept, and b is the Tafel slope. Tafel slope is a kinetic parameter used in determining the rate-determining step or mechanism involved during HER. The prime step in the many steps of HER is the hydrogen adsorption on the surface of the electrode by discharged protons. The primary process in the multiple-step HER is the discharged protons' adsorption on the electrode's surface, referred to as the Volmer step; this is followed by either Heyrovsky reaction, which is an electrodesorption step, or by the Tafel reaction, which is a hydrogen recombination step.

The HER in the alkaline medium is depicted as follows

$$\text{catalyst} + H_2O + e^- \rightarrow \text{catalyst}\,H_{ads} + OH^- \text{ (Volmer)} \tag{3}$$

$$\text{catalyst}H_{ads} + H_2O + e^- \leftrightarrow \text{catalyst} + H_2 + OH^- \text{ (Heyrovsky)} \tag{4}$$

(or)

$$2\text{catalyst} \leftrightarrow 2\text{catalyst} + H_2 \uparrow \text{ (Tafel)} \tag{5}$$

From the LSV curves, it was determined that the onset potentials for CrMX, MXene, and rGO at a current density of 1.0 mA cm^{-2} were −0.25, −0.53, and −0.62 V vs RHE, respectively. The HER kinetics of the electrocatalysts as prepared is

https://doi.org/10.1021/acsomega.3c03827
ACS Omega 2023, 8, 34768−34786

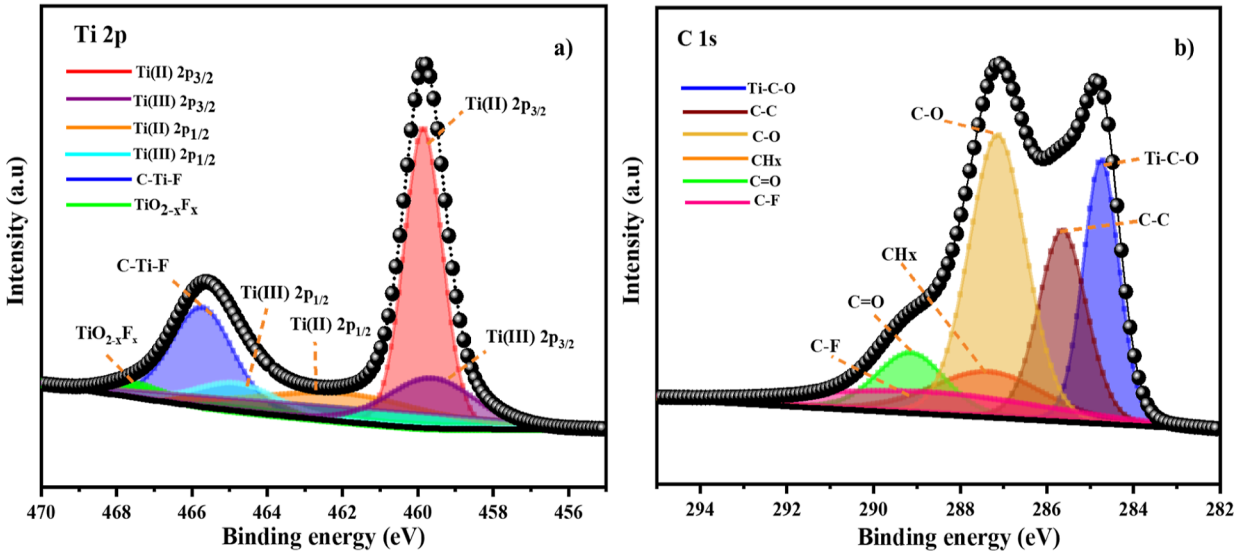

Figure 7. XPS spectra of (a) Ti 2p and (b) C 1s electron XPS spectra for the CrMX nanocomposite.

investigated using the Tafel slope analysis. rGO and MXene had higher Tafel slopes of 87.55 and 72.0 mV dec^{-1} exhibiting a lower electrocatalytic activity compared to that of CrMX with 56.64 mV dec^{-1} as seen in Figure 8b also with reference to bare NF.[62] The HER reaction of CrMX can be roughly thought to follow the Volmer−Heyrovsky mechanism with the Volmer step as the rate-determining step because the Tafel slope value of CrMX is in the range of 40−120 mV dec^{-1}. The rGO sheets intercalated within the MXene sheets in CrMX increases the surface area, thereby allowing the access of abundant active sites and leading to faster reaction kinetics.

Overpotential is referred to as an extra potential, which is required in electrochemical water splitting to overcome the intrinsic kinetic hindrance. η was determined using the following formulas

$$\eta = 0 - E_{RHE} \text{ for HER} \quad (6)$$

$$\eta = E_{RHE} - 1.229 \text{ for OER} \quad (7)$$

The HER overpotential of CrMX at 10 mA cm^{-2} current density is 360 mV, which is lower than those of MXene (547 mV) and rGO (630 mV) as shown in Figure 8c. The synergistic effect of MXene and rGO should be accountable for the enhanced performance of CrMX. The steps involved that contribute to the synergism are as follows: (i) adsorption of cetyltriammonium bromide (CTAB) on rGO, and CTA+ was evenly adsorbed onto the negatively charged rGO as a result of electrostatic interaction. (ii) Utilizing CTAB renders rGO partially hydrophilic by grafting the cationic head amino groups (NH_4^+), which attract the negatively charged MXene due to charged surface terminal groups (−OH, −F, and −O), resulting in a self-assembled multilayer. In addition to improving the compatibility between MXene and rGO, this ionic interaction process was able to achieve the right surface energy for CrMX as hydrophilic materials have high surface energy, which also results in increased electroactive sites.

Another parameter used to evaluate the electrocatalytic activity toward HER in electrochemical water splitting is the exchange current density (j_0). The ECSA must be known in order to use j_0 as a reliable indicator of the catalysts' intrinsic; thus, the values of exchange current density normalized with electrochemical active surface area. The values are summarized in Table 1. The resultant value indicated that intrinsic CrMX's charge-transfer efficiency is superior to those of both MXene and rGO electrodes.

For double-layer capacitance C_{dl} calculation of the three catalysts, cyclic voltammogram curves at varying scan rates in the non-Faradaic region were assayed. C_{dl} is directly proportional to the ECSA; the greater the C_{dl} value, the larger the ECSA, which means more active sites take part in the HER. CrMX has a higher C_{dl} value (3.02 mF cm^{-2}) than those of MX (1.65 mF cm^{-2}) and rGO (1.46 mF cm^{-2}). ECSA is calculated from C_{dl} values using the equation

$$\text{ECSA} = C_{dl}/C_S \quad (8)$$

An atomically smooth planar surface's specific capacitance in a given electrolytic medium is denoted by the symbol C_S. C_S was estimated to be 40 mF cm^{-2} for 1.0 M KOH in this study. Thus, the ECSAs of CrMX, MXene, and rGO electrodes are 75.5, 41.25, and 24.33 cm^2, respectively.

The roughness factor of the electrocatalysts is also derived from the electrochemical double-layer capacitance (C_{dl}) value as follows

$$\text{RF} = \frac{\text{ECSA}}{\text{geometric area of the electrode}} \quad (9)$$

Since the geometric area of the electrode (nickel foam) is 1 cm^2, the roughness factor is calculated to be 75.5, 41.25, and 24.33 for CrMX, MXene, and rGO, respectively.

In order to further explore how the electrochemically available sites affect the activity, the overpotential was plotted against log RF, which shows a linear variation of the synthesized catalysts as shown in Figure S11 and Table S1. As a result, it was confirmed that a sample's electrochemical performance is ought to be influenced by the number of accessible electrochemically active sites, and hence, the intrinsic activity of materials like exchange current density, where the current is normalized by the ECSA, gives a reflection of the electrocatalytic activity of the material and is more practical for water electrolysis.

CrMX exhibits a higher HER activity than that of others, implying that no restacking of interlayers occurs in CrMX, providing rich interfacial active sites. The chronoamperometric measurements were performed at an overpotential of −0.30 V

https://doi.org/10.1021/acsomega.3c03827
ACS Omega 2023, 8, 34768−34786

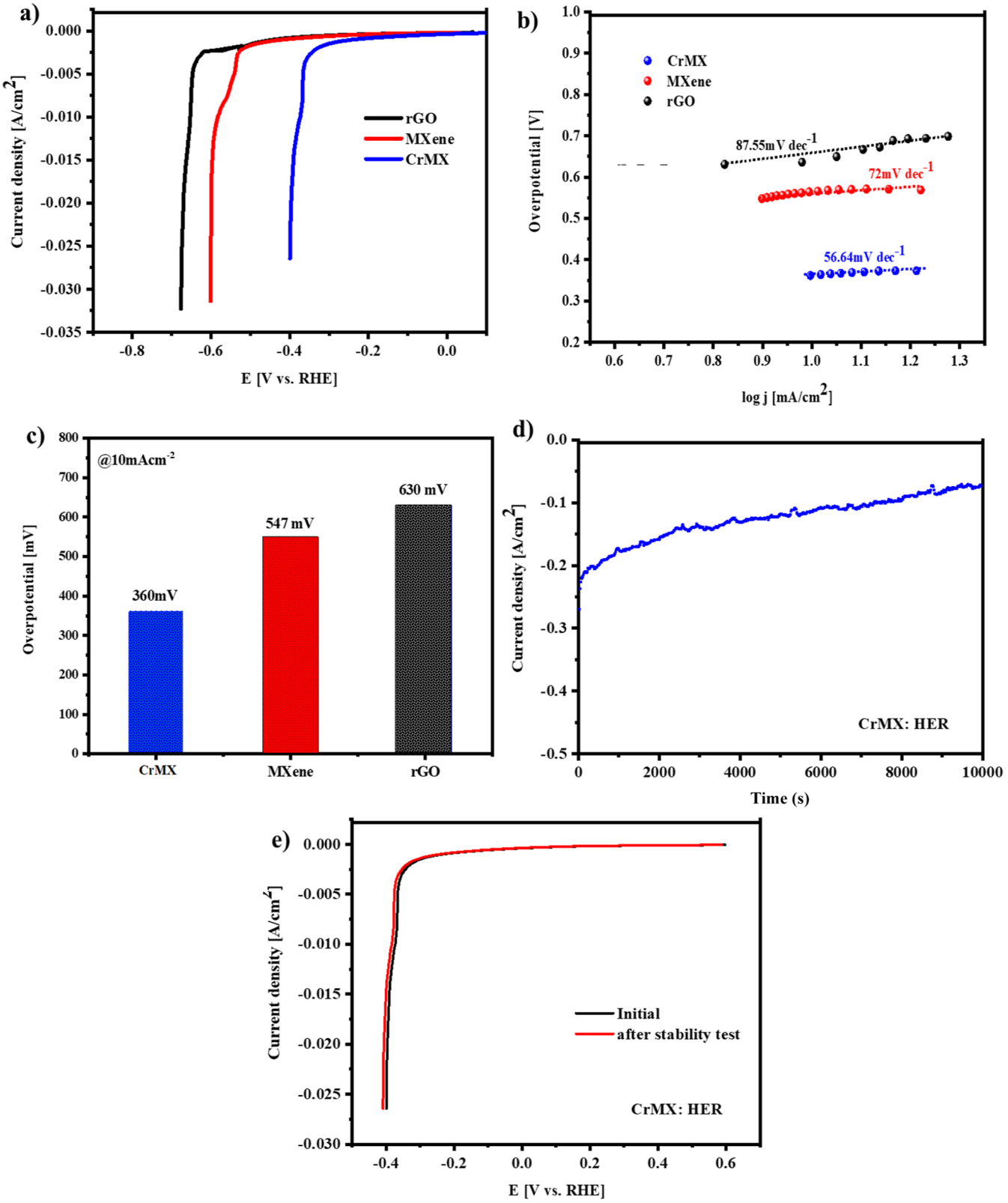

Figure 8. (a) *iR*-compensated HER polarization curves of different electrocatalysts in 1.0 M KOH at a scan rate of 5 mV s^{-1}; (b) corresponding Tafel plots of the catalysts. (c) Comparison of the overpotential of CrMX, MXene, and rGO in mV. (d) Long-term durability test of CrMX and (e) comparison of the stability of CrMX with an initial polarization curve before and after durability test in 1.0 M KOH.

(Figure 8d), once more confirming the long-term durability of the CrMX nanocomposite in the HER. After being used continuously for more than 10000 s, the material almost maintains (95.4%) its electrocatalytic behavior with a slight shift in potential seen initially for the HER according to the current density curve that is time-dependent and the cyclic voltammetric curves before and after CA measurements in Figure 8e. The

https://doi.org/10.1021/acsomega.3c03827
ACS Omega 2023, 8, 34768−34786

Table 1. Comparison of the Tafel Slope, Exchange Current Density, and Overpotential of CrMX in HER with 2D Materials from Other Works

	Tafel slope (mv dec^{-1})	exchange current (j_0) (A cm_{ECSA}^{-2})	overpotential (mV)	references
CrMX	56.64	1.152×10^{-6}	360	this work
MXene	72	7.66×10^{-12}	547	this work
rGO	87.55	6.16×10^{-13}	630	this work
20% Pt/C on nickel foam	48		40	63
Mo_2CT_x/2HMoS$_2$	60		119	64
TS-Ti_3C_2/CNT	73	0.017 mA cm^{-2}		65
PI/CNT-RGO	61	5.01 μA cm^{-2}	0.09 V	66
MoS_2QDS/RGO	63	0.699 mA cm^{-2}	63	67
MoP@C@rGO	79	0.67 mA cm^{-2}	168.9	68
CoS_2−C@MoS_2	61		173	69

slight shift in CrMX's catalytic activity can be attributed to material deterioration, surface passivation, or corrosion.

3.2.2. Electrochemical OER and Overall Water Splitting Activity. OER is typically the bottleneck for many energy technologies, including metal−air batteries. OER has sluggish kinetics and is a complicated and energy-intensive 4-e^- transfer process, which involves O═O bond formation and O−H bond breaking. An *iR* correction was used for further analysis because the as-measured current does not accurately reflect the catalysts' natural behavior as a result of ohmic resistance. The formula $\eta = E - 1.23$ V was used to calculate the OER overpotential. Figure 9a exhibits the polarization curves for the electrocatalysts demonstrating OER. CrMX outperforms the other catalysts by attaining a current density of 10 mA cm^{-2} at an overpotential of 179 mV, which is comparatively better that those of MXene (249 mV) and rGO (360 mV) with reference to RuO_2/NF (312 mV) from the work of Wang et al.[70] and bare nickel foam[71,72] (Figure 9c). By applying the Tafel equation to the LSV polarization curves, the Tafel plots were generated. With a Tafel slope of only 47.03 mV dec^{-1}, CrMX has the most favorable reaction kinetics for OER, while MXene has a Tafel slope of 171.9 mV dec^{-1}; rGO, 236.31 mV dec^{-1} ; and RuO_2/NF, 100 mV dec^{-1} (Figure 9b).

The first electron-transfer step was predicted to be the rate-determining step for OER with regard to the Tafel slope values, as shown below

$$M + OH^- \rightarrow MOH + e^- \tag{10}$$

where M is an acronym for the catalytically active site. It has been established that the enhanced kinetics coincide with the active sites' availability, which is established by the valuation of electrochemical double-layer capacitance (C_{dl}), which is again directly proportional to ECSA. The catalyst's sustainability is crucial to achieving an improved performance, in addition to the material's high catalytic activity. To assess the durability of the CrMX electrocatalysts, a chronoamperometric test was carried out. CrMX demonstrates excellent stability for 10000 s at a 1.3 V potential, and the LSV plot obtained subsequently to the stability test demonstrates nearly identical activity with a slight reduction in the current density (Figure 9d,e). The porous structure of CrMX on the nickel foam provides substantial availability of electrochemical active sites, but in addition, it aids the diffusion of O_2 that is in situ generated.

For overall water electrolysis, a two-electrode configuration utilizing CrMX as both cathode and anode was considered, drawing inspiration from the bifunctional behavior of the electrode material for both HER and OER. In a 1 M KOH solution, the CrMX electrolyzer, as depicted in Figure 9f, produces a current density of 10 mA cm^{-2} at a cell voltage of 1.78 V. At a cell voltage beyond 1.8 V, the gas bubbles released at the corresponding electrodes are shown in Figure 9f (inset).

Understanding the factors that contribute to better catalytic performance requires the quantification of the active sites.[73,74] It is thought that the Ti centers formed after oxidizing are the potential active sites for OER, HER, and overall water splitting catalysts. With the integration of the anodic peak obtained from the cyclic voltammogram and dividing it by the scan rate, it is possible to estimate the charge (Q) involved in the oxidation of the titanium species

$$Q = \frac{i}{\nu}\int_{E_1}^{E_2} i(E)\, dE \tag{11}$$

If most of the titanium centers are assumed to be catalytically active, the number of Ti(III) centers after oxidation from Ti(II) can be assessed, from which the number of active sites can be calculated, since only one electron is taking part in the oxidation reaction.

$$\text{Number of active sites} = \frac{Q}{1.60217662 \times 10^{-19}} \tag{12}$$

Thus, the number of electroactive sites responsible for the electrocatalysis of CrMX was calculated to be 2.36×10^{18} atoms cm^{-2}.

3.2.3. Electrochemical Evaluation of Supercapacitor Behavior. The energy storage performance was explored by testing the galvanostatic charge−discharge (GCD), cycling stability measurements, CV, and electrochemical impedance spectroscopy (EIS) of the electrodes with a three-electrode system in 1.0 M KOH. Figure 10a shows the *CV* curves of CrMX, MXene, and rGO on the nickel foam as positive electrodes at a scan rate of 50 mV s^{-1}. The CV curves of the CrMX and MXene composite contain a pair of obvious redox peaks, and the CV curve of rGO seems like a straight line due to high current density of the other two electrocatalysts. The chemical etching process results in mixed −OH, −O, and −F terminating groups on MXene surfaces. There is known to be little experimental control over the distribution of these functional groups on the surfaces.[75] There is abundant experimental evidence for the metallic properties of 2D MXenes with O* and OH* surface terminal groups, which support excellent charge transfer.[76] The redox peaks of the MXene-based electrocatalysts are possibly due to the alternating desorption and adsorption of the hydroxyl ions from the KOH electrolyte on the Ti_3C_2 nanosheets. The redox peak couple is accredited to the reversible redox reactions listed below[77,78]

https://doi.org/10.1021/acsomega.3c03827
ACS Omega 2023, 8, 34768−34786

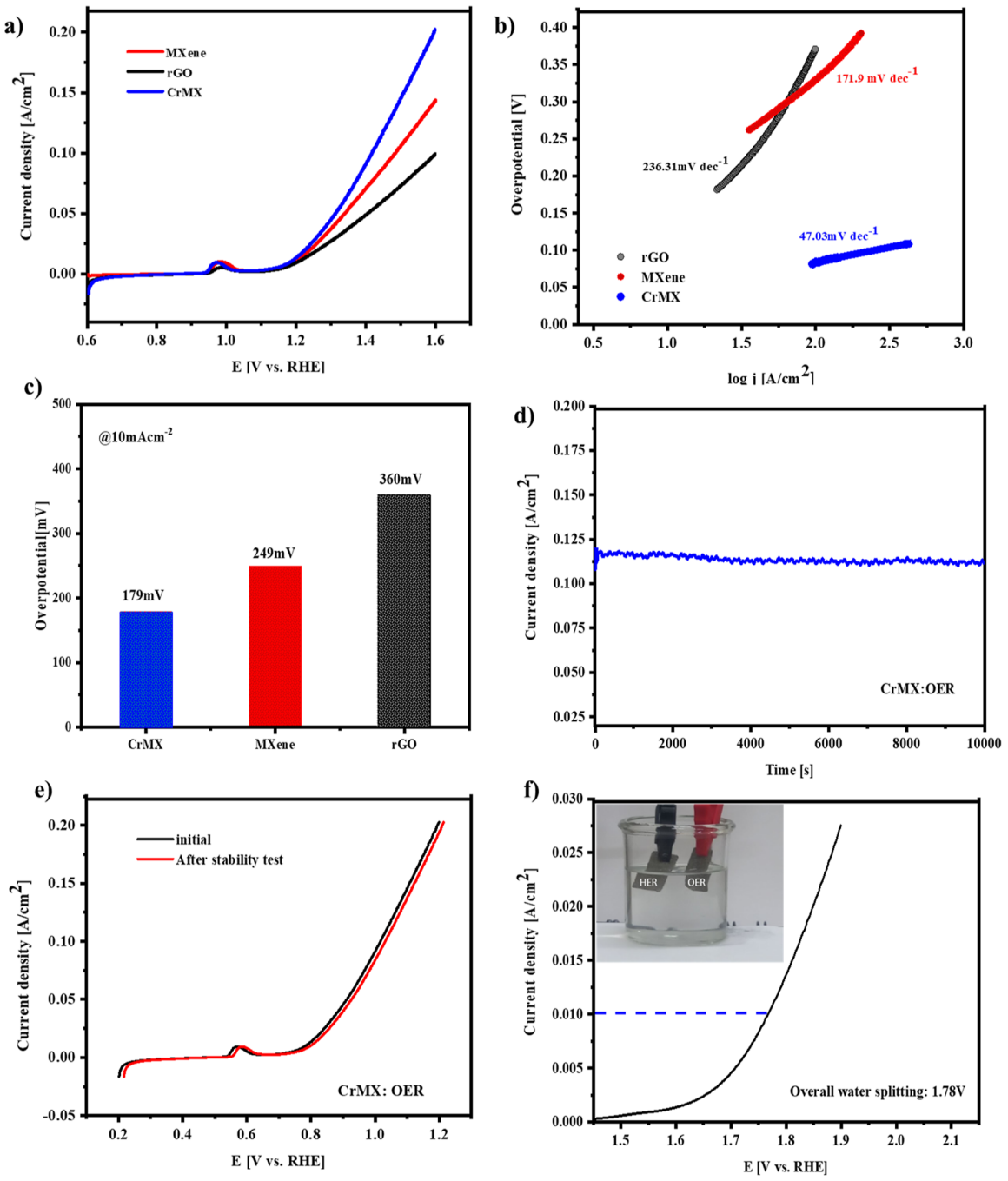

Figure 9. (a) *iR*-compensated OER polarization curves of different electrocatalysts in 1.0 M KOH at a scan rate of 5 mV s^{-1}; (b) corresponding Tafel plots of the three catalysts. (c) Comparison of the overpotential of CrMX, MXene, and rGO in mV, (d) long-term durability test of CrMX, (e) stability of CrMX with an initial polarization curve and after durability test in 1.0 M KOH, and (f) polarization curve of overall water splitting in 1.0 M KOH.

$$Ti_3C_2(OH)_x + OH^- \leftrightarrow Ti_3C_2(OH)_{x+1} + e^- \quad (13)$$

$$Ti_3C_2O_y + 2OH^- \leftrightarrow Ti_3C_2O_{y+1} + e^- + H_2O \quad (14)$$

In comparison to pristine MXene and rGO, the CrMX composite electrode exhibits the most integral area in cyclic voltammogram and the most significant enhancement in discharge time in GCD curves, demonstrating that the prevention of restacking of the MXene layers with the help of rGO is more favorable to improve the energy storage performance. This is attributed again to the combination of rGO and MXene, which is likely to provide access to the change in the valence state throughout electrochemical reactions in addition to facilitating the electrolyte diffusion and expanding the interlayer space of MXene.

The specific capacitance of CrMX, MXene, and rGO can be calculated from the cyclic voltammogram from the equation

$$C_{sp} = \frac{\int I \times dV}{v \times m \times V} \quad (15)$$

where specific capacitance is denoted with C_{sp}, I is the current, V is the applied potential window, A is the area of the active electrode, and v is the scan rate. The specific capacitance of CrMX is the highest at 652.0 F g^{-1}, while MXene is 411 F g^{-1} and rGO is 240 F g^{-1} at 0.5 A g^{-1}.

https://doi.org/10.1021/acsomega.3c03827
ACS Omega 2023, 8, 34768−34786

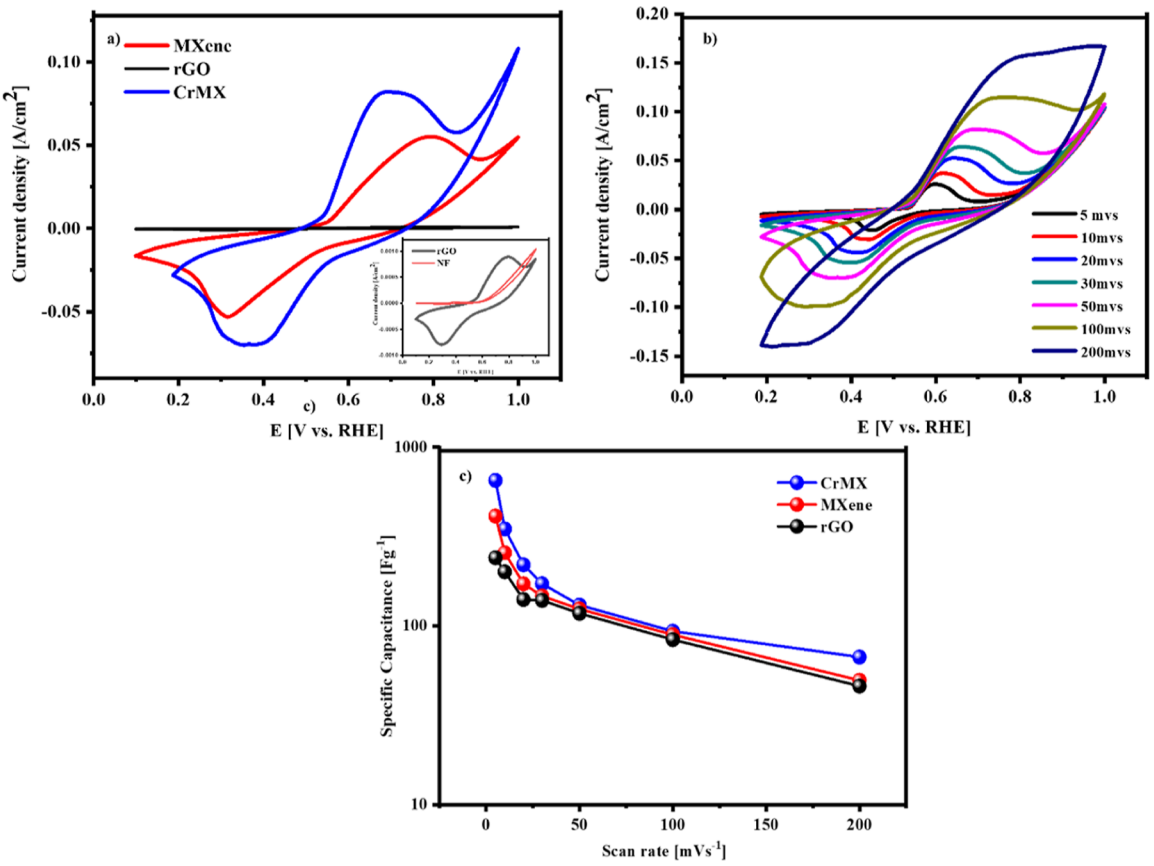

Figure 10. (a) Cyclic voltammograms of CrMX, MXene, and rGO on a nickel foam at a scan rate of 50 mV s^{-1} in 1.0 M KOH (inset of CV of rGO and NF), (b) cyclic voltammogram of CrMX in 1.0 M KOH at varying scan rates from 5 to 100 mV s^{-1}, and (c) capacitance vs scan rate curves based on *CV* data of CrMX, MXene, and rGO in KOH electrolyte.

The increase in the current density and area under the cyclic voltammetric curves with increasing scan rate was found to be caused by the pseudo-reversible reactions that stimulate the transfer of electron via the association/dissociation reactions.[79] The *CV* graph is asymmetric owing to the porous nature of the electrode inducing ohmic resistance and polarity. At lower scan rates, the ions present in the electrolytic solution have enough time to interact with the active area of the electrode material leading to increased specific capacitance, while due to insufficient time for interaction at higher scan rate, a lower specific capacitance is observed, as seen in Figure 10b,c. Cyclic voltammograms of (a) MXene and (b) rGO at varying current densities are provided in Figure S7.

The charging/discharging processes include small internal resistance (IR), and the resulting shape of CrMX in Figure 11a exhibits effective pseudo-capacitive performance; the same is observed for Figure S6a,b for MXene and rGO. The specific capacitance can be also calculated from the GCD curves using eq 2

$$C_{sp} = \frac{I \times \Delta t}{m \times V} \tag{16}$$

where the mass of the active material is represented as m, discharge time as Δt, applied potential window as V, discharge current as I, and specific capacitance as C_{sp}. The specific capacitances of CrMX, MXene, and rGO at a current density of 0.5 A g^{-1} are 544.50, 503.67, and 434.75 F g^{-1}, respectively, as seen in Figure S8. The CrMX electrode demonstrated excellent performance upon comparison with other reports as depicted in Table 2.

From Figure 11b,c, we can observe that as the current densities increase, the capacitance decreases due to less accessible area and deteriorating effect on the kinetics of the reaction at higher current densities. Thus, the redox activity and the greater ECSA of CrMX enhance their charge storage properties. The pseudocapacitive behavior is further confirmed from Figure 12a,b via Trasatti method from the equations

$$C^{-1} = k \times \nu^{0.5} + C^{T^{-1}} \tag{17}$$

$$C = k \times \nu^{-0.5} + C_{EDLC} \tag{18}$$

$$C_T = C_{PSUEDO} + C_{EDLC} \tag{19}$$

It is found that CrMX exhibits 96.54% psuedocapacitance and 3.46% electrical double-layer capacitance.

From the GCD data, the energy (W h kg^{-1}) and power density P (W kg^{-1}) were derived and calculated based on the following equation

$$E = \frac{C \times \Delta\nu^2 \times 1000 \times 1/2}{3600} \tag{20}$$

$$P = \frac{E \times 3600}{\Delta t} \tag{21}$$

where Δt is the discharge time and ΔV is the potential window of discharge. CrMX exhibited a maximum power density of 312.49 W kg^{-1} at an energy density of 18.91 W h kg^{-1}; for MXene, a

https://doi.org/10.1021/acsomega.3c03827
ACS Omega 2023, 8, 34768−34786

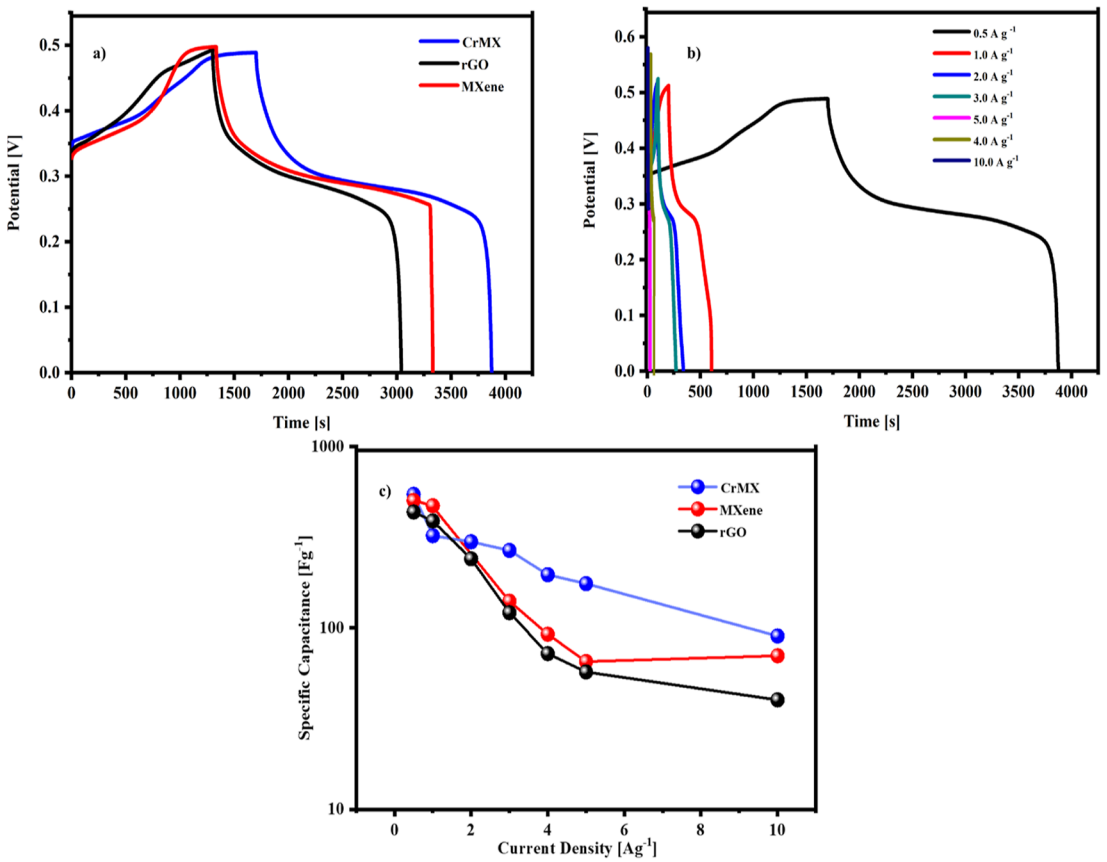

Figure 11. (a) Galvanostatic charge/discharge curve of CrMX, rGO, and MXene at 0.5 A g^{-1} current density in 1.0 M KOH, (b) galvanostatic charge−discharge curve of CrMX at varying current densities, and (c) capacitance vs current density curves based on the GCD data of CrMX, rGO, and MXene in KOH electrolyte.

Table 2. Comparison of Specific Capacitance of CrMX with Those of 2-Dimensional Materials from Other Works

	specific capacitance (F/g)	electrolyte	current density (A g^{-1})	references
CrMX	544.50	1.0 M KOH	0.5	this work
MXene	124	KOH		80
Nb-doped MXene	442.7	6 M KOH		81
N-rGO/MWCNTs/NF	142	KOH	1	82
S-rGO	392	Na_2SO_4	0.04	83
MrGO	163	KOH	1	84
(RGO)/poly(3,4-ethylenedioxythiophene)	213	1 M H_2SO_4	0.5	85
PEDOT30/MX	335	poly(vinyl alcohol) (PVA)/H_3PO_4 gel electrolyte	scan rate of 10 mV s^{-1}	86

power density of 303.46 W h kg^{-1} was noted at an energy density 17.49 W h kg^{-1}, and for rGO, a power density of 295.50 W h kg^{-1} was noted at an energy density 15.10 W h kg^{-1}, and the Ragone plot comparing our work with other works is given in Figure 13 and Table S2.

The EIS was done to analyze the kinetics as well as the charge transfer and solution kinetics of the electrocatalytic materials. The impedance was studied over a frequency range from 100 kHz to 0.01 Hz with an AC amplitude of 10 mV, and the data in Figure 14 show the presence of a partial semicircle because of the charge-transfer resistance of the synthesized electrocatalysts. The solution resistanceR_s values are 1.03, 1.8, and 2.5 Ω cm^2.

The R_s value for CrMX is lower compared to that for MXene, which can be owing to the presence of rGO and its effect on MXene's conductivity. The inset showcases the suggested equivalent circuit for CrMX, which is made up of three sets of serial elements that each describe a specific material's or interface's resistive or capacitive behavior. In the equivalent circuit, R_s represents the sum of the high-frequency resistances like solution resistance due to the electrolyte and/or resistance to the Nickel foam. A parallel $R-C$ element is denoted as R_p and CPE. The $R-C$ elements are often used to describe the combined resistive and capacitive behavior of a material or an interface within an electrochemical device. Here, R_p is the electrical resistance involved in the adsorption of OH− on the nickel foam, and CPE is the electric double-layer capacitance existing at the CrMX−nickel foam interface. The diffusion resistance is attributed by the Warburg element.

The stability of CrMX was assessed by GCD at a current density of 10 A g^{-1} before and after the discharge time, which was retained even after 5000 cycles with a capacitance percentage of 87%. Thus, rGO's confinement within the layers of MXene corroborates its outstanding performance rate that

https://doi.org/10.1021/acsomega.3c03827
ACS Omega 2023, 8, 34768−34786

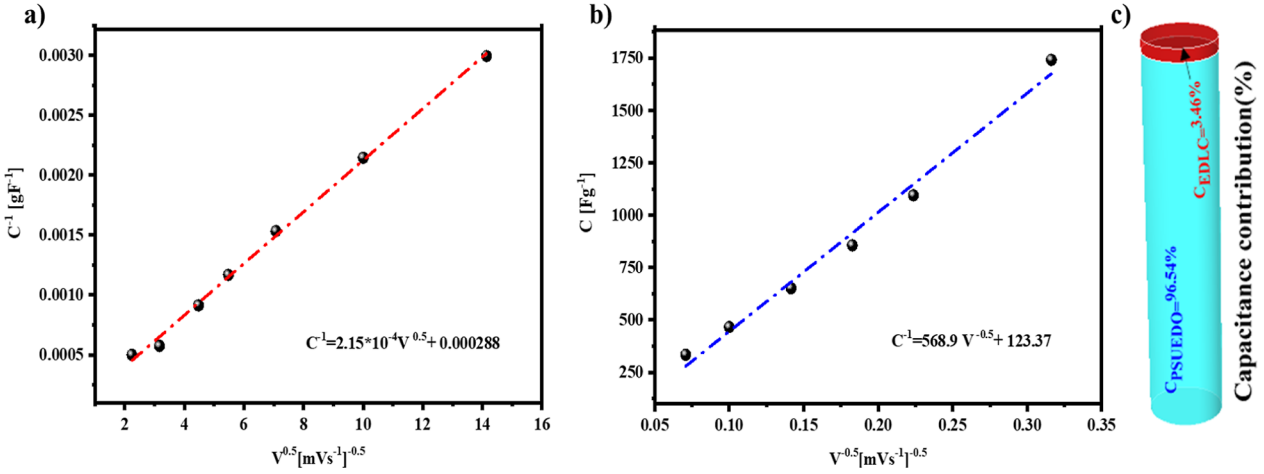

Figure 12. (a) The plot depicts the gravimetric capacitance reciprocal (C^{-1}) versus scan rate square root ($v^{0.5}$). (b) The plot demonstrates the gravimetric capacitance (C) versus square root of scan rate reciprocal ($v^{-0.5}$). (c) Psuedocapacitance (%) and electric double-layer capacitance (%) of CrMX via the Trasatti method. (c) Capacitance contribution % of CrMX.

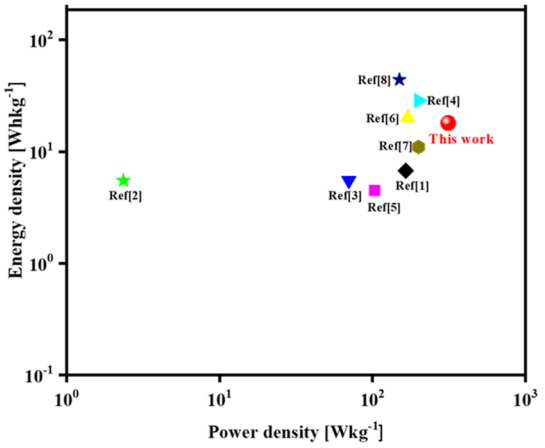

Figure 13. Comparison of power and energy densities of the CrMX supercapacitor to those in other works in the Ragone plot.

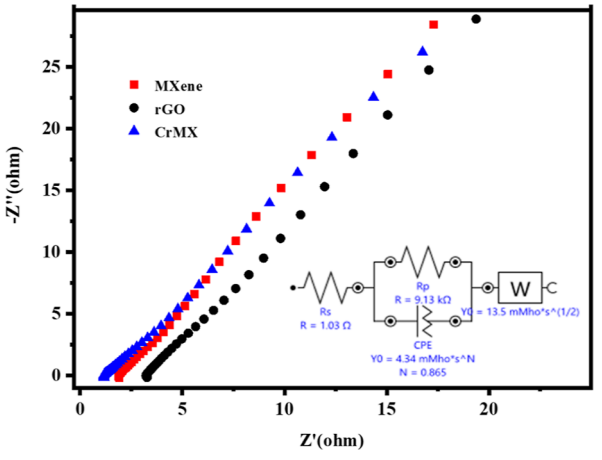

Figure 14. Nyquist plots of CrMX, MXene, and rGO and the inset contains the equivalent circuit of CrMX.

illustrates the stability of CrMX even after 5000 cycles under a current density (10 A g^{-1}) in Figure S9.

3.2.4. CrMX as the Electrocatalyst for MOR in DMFC Application. This section of the article deliberates the electrocatalytic properties of the fabricated electrodes toward methanol oxidation. As observed earlier, CrMX exhibits a larger peak current, a greater enclosed CV area, and a higher peak current than those of MXene and rGO based on the CV recorded in 1 M KOH in Figure 10a. This result affirms the CrMX electrode's solid Faradaic properties, which are anticipated to offer enough electroactive sites for MOR. There is a clear indication of the oxidation (0.68 V) and reduction peaks (0.38 V) of CrMX in the cyclic voltammogram of the electrode materials attained when methanol is absent. The peaks are attributed to the electron transition, which is reversible between CTAB-rGO-intercalated $Ti_3C_2O_2$ and $Ti_3C_2(OH)_x$.

Methanol is first adsorbed on the catalyst surfaces during heterogeneous catalysis, and methanol is then converted into the last products through a series of intermediate species. The sudden increase in the oxidation peak current density in the forward scan indicated that methanol was electrooxidizing. A more drastic increase in the anodic peak current was noted with the addition of methanol, which ensures the methanol oxidation compared to that without methanol at 50 mV s^{-1} from the *CV* curves of CrMX in Figure 16a. According to the *CV* graphs, the peak current density was 104.15 mA cm^{-2} without methanol, while it was 373.60 mA cm^{-2} with methanol. This outcome attests to the CrMX catalyst's excellent catalytic activity.

The following is a proposed electron transfer mechanism for the MOR at the CrMX catalyst surface in alkaline media, as shown in Figure 15

$$\mathrm{CrMX} + \mathrm{CH_3OH} \rightarrow \mathrm{CrMX} - \mathrm{CH_3OH_{ads}} \quad (22)$$

$$\mathrm{CrMX} - \mathrm{CH_3OH_{ads}} + 2\mathrm{OH^-} \rightarrow \mathrm{CrMX} - (\mathrm{CO})_{ads} + 3\mathrm{H_2O} + 2\mathrm{e^-} \quad (23)$$

$$\mathrm{CrMX} + \mathrm{OH^-} \rightarrow \mathrm{CrMX} - \mathrm{OH_{ads}} + \mathrm{e^-} \quad (24)$$

$$\mathrm{CrMX} - \mathrm{CO_{ads}} + \mathrm{CrMX} - \mathrm{OH_{ads}} + \mathrm{OH^-} \rightarrow \mathrm{CrMX} + \mathrm{CO_2} + \mathrm{H_2O} + \mathrm{e^-} \quad (25)$$

Methanol is adsorbed on the surface of the electrocatalyst in the first step. Here, both MXene and rGO provide edge sites and large surface area for the methanol adsorption. The decomposition of the adsorbed methanol to carbonaceous materials such as CO, COH, CHOH, and CH_2OH occurs in the second

https://doi.org/10.1021/acsomega.3c03827
ACS Omega 2023, 8, 34768−34786

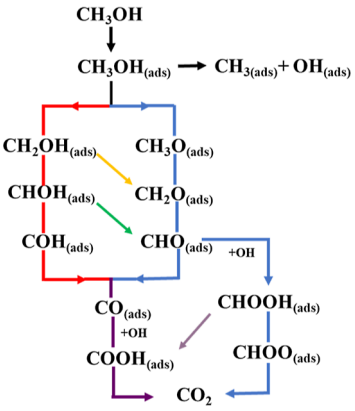

Figure 15. Every conceivable route for methanol oxidation on the catalyst surface.

step. The OH^- ions of the alkaline metals are also adsorbed, aiding the oxidation of the CO adsorbed and thereby regenerating the catalysts' active sites. The type and surface density of the oxygen-containing groups that are still covalently bound to the rGO support also contribute to the enhanced electroactivity of CrMX. The available oxygen groups on the reduced graphene may facilitate the bifunctional mechanism by which the adsorbed CO, or CO_{ads}, on MXene is oxidized. Water molecules dissociatively adhere to rGO, forming rGO-(OH)ads surface groups close to the transition metal Ti, which quickly oxidize the CO_{ads} groups on the periphery of the material.[87] It is most probable that the synergistic effect of rGO and MXene increases the adsorption of OH_{ads} and improves the stability and activity of CrMX; thus, CrMX had the maximum current density in 1 M KOH + 1.0 M CH_3OH at 373.60 mA cm^{-2} compared to that in MXene at 221.49 mA cm^{-2} and rGO at 165.25 mA cm^{-2}, as observed in Figure 16a.

The effect of varying scan rate for methanol electrooxidation of CrMX was studied in 1 M KOH + 1.0 M CH_3OH (Figure 17a). When the scan rate was varied from 5 to 200 mV s^{-1}, the current density also increased for the electrode with no shift in the oxidation peak potential. The relationship between scan rate square root and the oxidation peak current density is roughly linear, indicating that the methanol oxidation process using a CrMX-based electrode is a diffusion-controlled process (Figure 17b). As methanol concentrations were varied from 0.5 to 2.0 M at a scan rate of 50 mV s^{-1}, the voltammetric profile of methanol is recorded, and it was observed that as the methanol concentration increases, the current density also increases (Figure 17c). The correlation between the methanol concentration and current density was examined, as shown in Figure 17d. It is also interesting to note that CrMX is stable and that its surface is not harmed by the carbonaceous intermediates produced during the oxidation process since the anodic peak potential does not change with the increase in the concentration of methanol.

Chronoamperometric studies were carried out for 1 h at a constant potential of 0.55 V in 1.0 M CH_3OH and 1.0 M KOH solutions to test the endurance of the composite electrodes. Figure 18a illustrates the current−time responses of all three electrocatalysts. The oxidation current drops initially and stabilizes to a constant value. CrMX, MXene, and rGO exhibited initial current densities of 46.46, 34.63, and 7.614 mA cm^{-2}. However, MXene and rGO decayed faster compared to the final electrocatalyst, indicating the lower stability of these systems; the adsorbed intermediates like CO and HCOOH during the methanol electrooxidation reaction are attributed to the current decay for all electrodes.

The electrochemical activity of the electrode is well known to be dependent on its charge transfer or the rate of electron transfer characteristics. Here, we investigate EIS of CrMX with and without 1.0 M methanol in a 1 M KOH electrolyte with and without 0.5 M methanol to study how the charge transfer kinetics are affected by methanol and was measured within a frequency range from 100 kHz to 0.01 Hz with an AC amplitude of 10 mV. Both Nyquist plots show a a semicircle at a high-frequency region, while in the low-frequency region, a straight line was seen. The starting point of a semicircle on the real axis of a high-frequency region and the straight line in the low-frequency region correspond to the resistance of the electrolyte and diffusion resistance, respectively (Figure 18b). After the addition of methanol, the charge transfer and electrolytic resistance slightly increase due to the adsorption of the intermediates on the electrode's surface, which is also the reason behind the decay in current seen in the chronoamperometric curves. The comparison of the cyclic stability of CrMX in

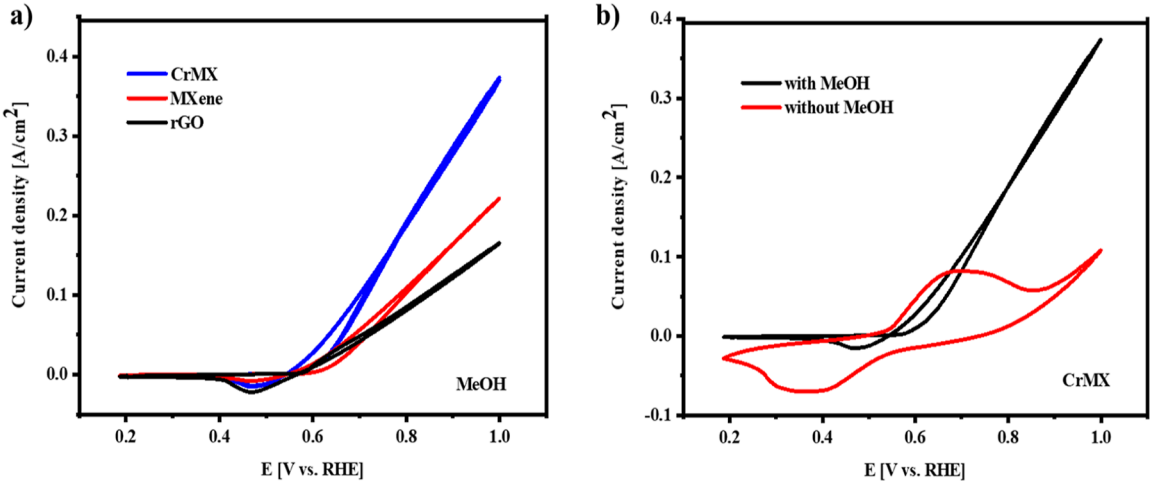

Figure 16. (a) Cyclic voltammogram of all the electrocatalysts in 1 M KOH + 1.0 M methanol at a scan rate of 50 mV s^{-1} and (b) comparison of CrMX in the presence and absence of methanol at a scan rate of 50 mV s^{-1}.

https://doi.org/10.1021/acsomega.3c03827
ACS Omega 2023, 8, 34768−34786

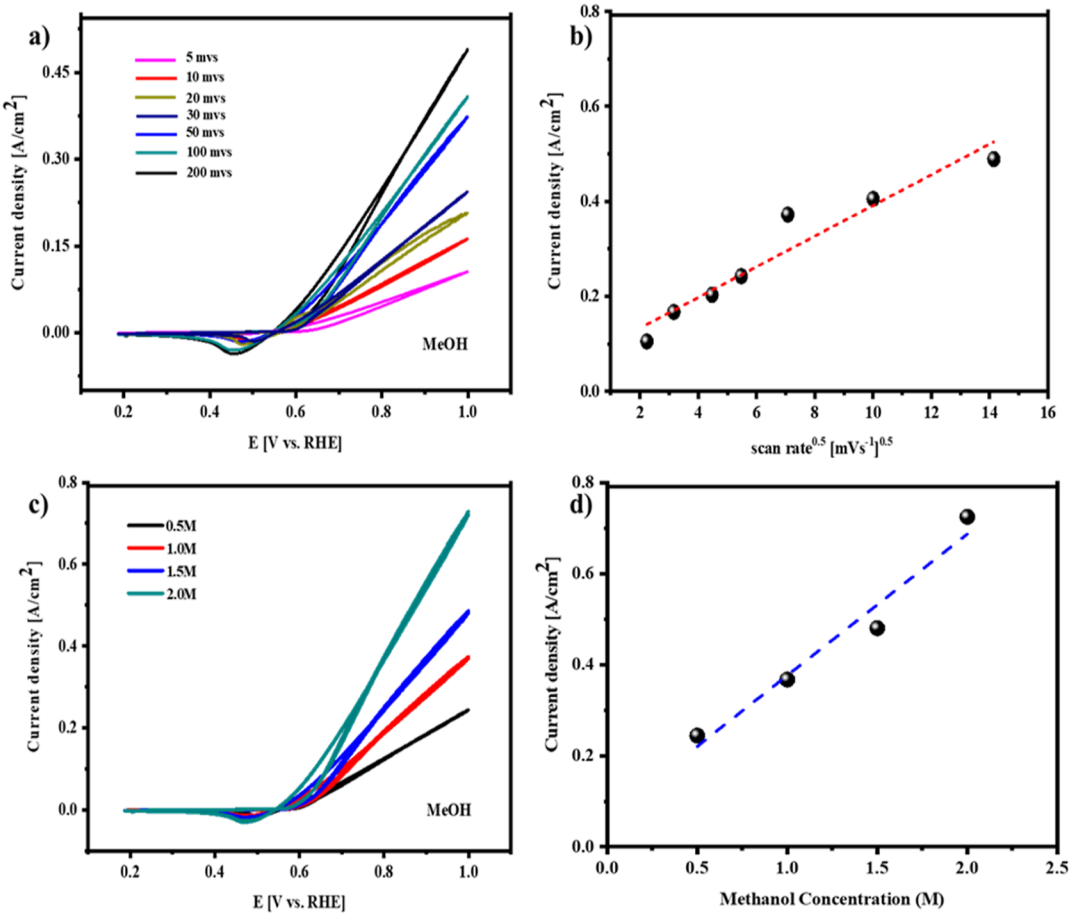

Figure 17. (a) Cyclic voltammogram of CrMX at varying scan rates such as 5, 10, 20, 30, 50, 100, and 200 mV/s in 0.1 M KOH + 1.0 M methanol. (b) Relationship between the current density and the scan rate square root. (c) *CV* plot of MOR with CrMX in the presence of different methanol concentrations 0.5−2.0 M in 1.0 M KOH at a scan rate of 50 mV s^{-1}.

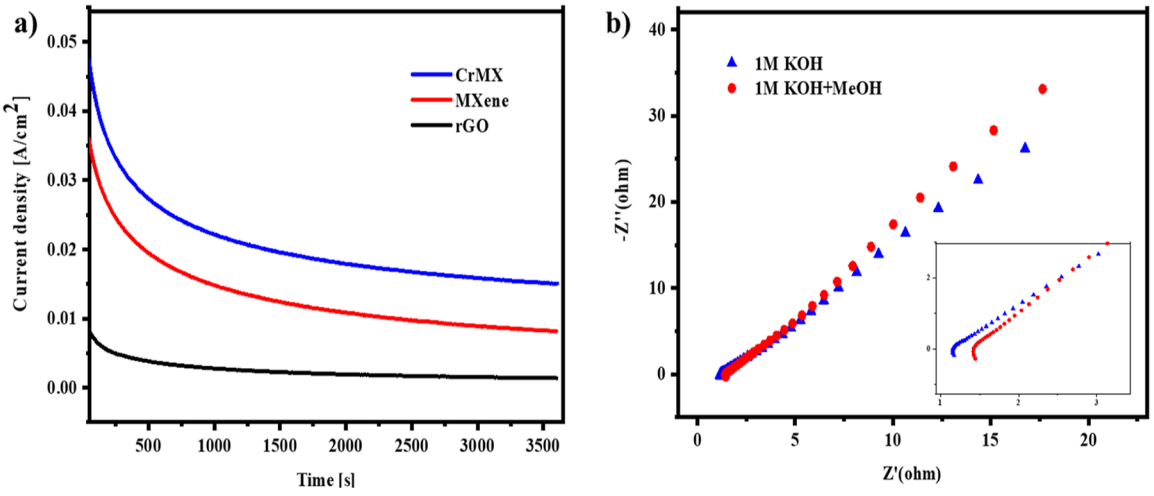

Figure 18. (a) Chronoamperometric curves of CrMX, MXene, and rGO electrode. (b) Nyquist plots of CrMX in the presence and absence of 1 M methanol along with the inset.

1 M KOH + 1 M methanol after 400 cycles is depicted in Figure S10.

4. CONCLUSIONS

A facile and binder-free CTAB-rGO-modified MXene hybrid film on a nickel foam was synthesized via layer-by-layer assembly and dip-coating technique, and their electrochemical activity for hydrogen evolution, oxygen evolution, supercapacitor, and DMFC applications was analyzed. The properties of the as-prepared electrocatalysts were investigated using various physiochemical characterizations such as XRD studies, SEM, TEM, XPS, BET, and FTIR analysis. For the electrochemical studies, the electrocatalyst CrMX exhibited a current density of 10 mA cm^{-2} and a low overpotential (η) of 360 V with the

https://doi.org/10.1021/acsomega.3c03827
ACS Omega 2023, 8, 34768−34786

electrochemical desorption as the rate-determining step due to a Tafel slope value of 56.6 mV/dec for HER and an overpotential (η) 179 mV and a Tafel slope value of 47.03 mV/dec at a current density of 10 mA cm^{-2} for OER in an alkaline medium. Taking advantage of the porous networks of both MXene and rGO for fast charge and mass transport leads to a higher oxidation current density of 373.60 mA cm^{-2} toward MOR compared to those by MXene at 221.49 mA cm^{-2} and rGO at 165.25 mA cm^{-2} as the anode catalyst for DMFC. CrMX also showcased a high volumetric capacitance of 544.50 F g^{-1} at a current density of 0.5 A g^{-1} as the supercapacitor electrode with a good capacity retention of 87% during 5000 cycles. This work highlights the significance of the CTAB-rGO-modified MXene hybrid film on the nickel foam to demonstrate its multifunctional activity for energy conversion and storage devices, thus showcasing the versatility of the synthesized catalyst to be utilized in commercial electrochemical applications.

■ ASSOCIATED CONTENT

Supporting Information

The Supporting Information is available free of charge at https://pubs.acs.org/doi/10.1021/acsomega.3c03827.

SEM images and EDX of MAX phase, rGO, and MXene; XPS spectra; BET isotherms; GCD curves and CVs of MXene and rGO at varying current densities; specific capacitance comparison; capacitance retention % vs cycle number of CrMX; CrMX cyclic stability in 1 M KOH + 1 M methanol after 400 cycles; potential vs log RF @ 10 mA cm^{-2}; comparison of ECSA and roughness factor among rGO, MXene, and CrMX; and comparison of electrochemical results with other 2D materials (PDF)

■ AUTHOR INFORMATION

Corresponding Author

Ragupathy Dhanusuraman − *Nano Electrochemistry Lab (NEL), Department of Chemistry, National Institute of Technology Puducherry, Karaikal 609609, India;* orcid.org/0000-0002-4260-2347; Email: ragu.nitpy@gmail.com, ragu@nitpy.ac.in

Authors

Asha Raveendran − *Nano Electrochemistry Lab (NEL), Department of Chemistry, National Institute of Technology Puducherry, Karaikal 609609, India;* orcid.org/0000-0002-6790-0201

Mijun Chandran − *Department of Chemistry, Central University of Tamil Nadu, Thiruvarur 610005, India;* orcid.org/0000-0002-3921-8491

Masoom Raza Siddiqui − *Chemistry Department, College of Science, King Saud University, Riyadh 11451, Saudi Arabia*

Saikh Mohammad Wabaidur − *Chemistry Department, College of Science, King Saud University, Riyadh 11451, Saudi Arabia*

Muthusankar Eswaran − *Division of Systems and Synthetic Biology, Department of Biology and Biological Engineering, Chalmers University of Technology, Göteborg 41296, Sweden;* orcid.org/0000-0001-9962-5817

Complete contact information is available at: https://pubs.acs.org/10.1021/acsomega.3c03827

Notes

The authors declare no competing financial interest.

■ ACKNOWLEDGMENTS

Authors are grateful to the Researchers Supporting project number (RSP2023R326), King Saud University, Riyadh, Saudi Arabia. Also, the authors would like to thank the basic research support from the National Institute of Technology Puducherry, Karaikal, India.

■ REFERENCES

(1) Dong, W.; Xiao, H.; Jia, Y.; Chen, L.; Geng, H.; Bakhtiar, S. U. H.; Fu, Q.; Guo, Y. Engineering the Defects and Microstructures in Ferroelectrics for Enhanced/Novel Properties: An Emerging Way to Cope with Energy Crisis and Environmental Pollution. *Advanced Science* **2022**, *9*, 2105368.

(2) Madaswamy, S. L.; Vengadesan, K.; Wabaidur, S. M.; Islam, M. A.; Philips, M. F.; Dhayalan, V.; Dhanusuraman, R. One-pot electro-co-deposition of nanospherical polydiphenylamine-palladium−supported graphitic carbon nitride nanohybrid for efficient methanol oxidation. *Ionics* **2022**, *28*, 4697−4708.

(3) Sankar Sivasankarapillai, V.; Veni Keertheeswari, N.; Chahal, P.; Mohammad Wabaidur, S.; Ponnusamy, V. K.; Dhanusuraman, R. Facile electrodeposition fabrication of raspberry-like gold microspheres decorated polydiphenylamine nanohybrid coated electrode for efficient direct methanol fuel cell application. *Fuel* **2022**, *330*, 125530.

(4) Chokkiah, B.; Eswaran, M.; Alothman, A. A.; Alsawat, M.; Ifseisi, A. A.; Alqahtani, K. N.; Dhanusuraman, R. Facile fabrication of hollow polyaniline/carbon nanofibers-coated platinum nanohybrid composite electrode as improved anode electrocatalyst for methanol oxidation. *J. Mater. Sci.: Mater. Electron.* **2022**, *33*, 8768−8776.

(5) Veni Keertheeswari, N.; Madaswamy, S. L.; Chokkiah, B.; Albaqami, M. D.; Wabaidur, S. M.; Lee, S. C.; Dhanusuraman, R. Synthesis of polydiphenylamine nanostructures via microwave and ultra-sonication method for supercapacitor performance. *J. Mater. Sci.: Mater. Electron.* **2022**, *33*, 23236−23249.

(6) Raveendran, A.; Chandran, M.; Mohammad Wabaidur, S.; Ataul Islam, M.; Dhanusuraman, R.; Ponnusamy, V. K. Facile electrochemical fabrication of Nickel-Coated Polydiphenylamine (Ni/PDPA) nanocomposite material as efficient anode catalyst for direct alcohol fuel cell application. *Fuel* **2022**, *324*, 124424.

(7) Vrabie, C. Electric Vehicles Optimism versus the Energy Market Reality. *Sustainability* **2022**, *14*, 5388.

(8) Dong, J.; Bauman, J. Maximizing Driving Range for Fuel Cell Range Extender Vehicles with Fixed Energy Storage Costs. *IEEE Trans. Transp. Electrif.* **2023**, *9*, 1042−1059.

(9) Chandran, M.; Thomas, A.; Raveendran, A.; Vinoba, M.; Bhagiyalakshmi, M. MoS2 confined MXene heterostructures as electrode material for energy storage application. *J. Energy Storage* **2020**, *30*, 101446.

(10) Chandran, M.; Shamna, I.; Anusha, A.; Bhagiyalakshmi, M. Synthesis of mesoporous carbon-polymeric hybrid material for energy storage application. *SN Appl. Sci.* **2019**, *1*, 509.

(11) Wu, Z.; Jiang, L.; Tian, W.; Wang, Y.; Jiang, Y.; Gu, Q.; Hu, L. Novel sub-5 nm layered niobium phosphate nanosheets for high-voltage, cation-intercalation typed electrochemical energy storage in wearable pseudocapacitors. *Adv. Energy Mater.* **2019**, *9*, 1900111.

(12) Chandran, M.; Raveendran, A.; Vinoba, M.; Vijayan, B. K.; Bhagiyalakshmi, M. Nickel-decorated MoS2/MXene nanosheets composites for electrocatalytic oxidation of methanol. *Ceram. Int.* **2021**, *47*, 26847−26855.

(13) Huang, H.; Yang, S.; Vajtai, R.; Wang, X.; Ajayan, P. M. Pt-decorated 3D architectures built from graphene and graphitic carbon nitride nanosheets as efficient methanol oxidation catalysts. *Adv. Mater.* **2014**, *26*, 5160−5165.

(14) Gong, Q.; Cheng, L.; Liu, C.; Zhang, M.; Feng, Q.; Ye, H.; Zeng, M.; Xie, L.; Liu, Z.; Li, Y. Ultrathin $MoS_{2(1-x)}Se_{2x}$ Alloy Nanoflakes For Electrocatalytic Hydrogen Evolution Reaction. *ACS Catal.* **2015**, *5*, 2213−2219.

(15) Zhang, W.; Lai, W.; Cao, R. Energy-related small molecule activation reactions: oxygen reduction and hydrogen and oxygen

evolution reactions catalyzed by porphyrin-and corrole-based systems. *Chem. Rev.* **2017**, *117*, 3717−3797.
(16) Deng, X.; Zhang, E.; Lei, J.; Jia, D.; Liu, Y.; Shuchao, H. Numerical Study on the Effect of an Improved Three-Partition Baffle Flow Field on Proton Exchange Membrane Fuel Cell Performance. *ACS Omega* **2022**, *7*, 42872−42882.
(17) Kumaravel, S.; Subramanian, M.; Karthick, K.; Sakthivel, A.; Kundu, S.; Alwarappan, S. DNA-Modified Cobalt Tungsten Oxide Hydroxide Hydrate Nanochains as an Effective Electrocatalyst with Amplified CO Tolerance during Methanol Oxidation. *ACS Omega* **2021**, *6*, 19162−19169.
(18) Yang, X.; Xue, J.; Feng, L. Pt nanoparticles anchored over Te nanorods as a novel and promising catalyst for methanol oxidation reaction. *Chem. Commun.* **2019**, *55*, 11247−11250.
(19) Meenu, P. C.; Roy, S.; Chakraborty, C.; Roy, S. Electro catalytic oxidation reactions for harvesting alternative energy over non noble metal oxides: Are we a step closer to sustainable energy solution? *Adv. Powder Technol.* **2021**, *32*, 2663−2689.
(20) Chen, J.; Wang, X.; Wang, J.; Lee, P. S. Sulfidation of NiMn-layered double hydroxides/graphene oxide composites toward supercapacitor electrodes with enhanced performance. *Adv. Energy Mater.* **2016**, *6*, 1501745.
(21) Shan, J.; Zheng, Y.; Shi, B.; Davey, K.; Qiao, S.-Z. Regulating electrocatalysts via surface and interface engineering for acidic water electrooxidation. *ACS Energy Lett.* **2019**, *4*, 2719−2730.
(22) Zhang, J.; Ding, J.; Li, C.; Li, B.; Li, D.; Liu, Z.; Cai, Q.; Zhang, J.; Liu, Y. Fabrication of novel ternary three-dimensional RuO2/graphitic-C3N4@ reduced graphene oxide aerogel composites for supercapacitors. *ACS Sustain. Chem. Eng.* **2017**, *5*, 4982−4991.
(23) Fan, W.; Shi, Y.; Gao, W.; Sun, Z.; Liu, T. Graphene−carbon nanotube aerogel with a scroll-interconnected-sheet structure as an advanced framework for a high-performance asymmetric supercapacitor electrode. *ACS Appl. Nano Mater.* **2018**, *1*, 4435−4441.
(24) Yan, J.; Ren, C. E.; Maleski, K.; Hatter, C. B.; Anasori, B.; Urbankowski, P.; Sarycheva, A.; Gogotsi, Y. Flexible MXene/graphene films for ultrafast supercapacitors with outstanding volumetric capacitance. *Adv. Funct. Mater.* **2017**, *27*, 1701264.
(25) Dhanusuraman, R.; Chahal, P.; Raveendran, A.; Hossain, M.; Alshgari, R. A.; Wabaidur, S. M.; Eswaran, M. Facile fabrication of platinum loaded poly (2, 5-dimethoxy aniline)/activated carbon ternary nanocomposite as an efficient electrode material for high performance supercapacitors. *J. Energy Storage* **2023**, *60*, 106554.
(26) Luo, Y.; Li, X.; Cai, X.; Zou, X.; Kang, F.; Cheng, H.-M.; Liu, B. Two-dimensional MoS2 confined Co (OH) 2 electrocatalysts for hydrogen evolution in alkaline electrolytes. *ACS Nano* **2018**, *12*, 4565−4573.
(27) Zhao, M.; Zhang, J.; Xiao, H.; Hu, T.; Jia, J.; Wu, H. Facile in situ synthesis of a carbon quantum dot/graphene heterostructure as an efficient metal-free electrocatalyst for overall water splitting. *Chem. Commun.* **2019**, *55*, 1635−1638.
(28) Davodi, F.; Tavakkoli, M.; Lahtinen, J.; Kallio, T. Straightforward synthesis of nitrogen-doped carbon nanotubes as highly active bifunctional electrocatalysts for full water splitting. *J. Catal.* **2017**, *353*, 19−27.
(29) Kakati, N.; Maiti, J.; Lee, S. H.; Jee, S. H.; Viswanathan, B.; Yoon, Y. S. Anode catalysts for direct methanol fuel cells in acidic media: do we have any alternative for Pt or Pt−Ru? *Chem. Rev.* **2014**, *114*, 12397−12429.
(30) Xia, B. Y.; Wu, H. B.; Wang, X.; Lou, X. W. One-pot synthesis of cubic PtCu3 nanocages with enhanced electrocatalytic activity for the methanol oxidation reaction. *J. Am. Chem. Soc.* **2012**, *134*, 13934−13937.
(31) Chandran, M.; Raveendran, A.; Thomas, A.; Vinoba, M.; Jeong, S. K.; Bhagiyalakshmi, M. Nickel decorated on Platinum Confined in MXene as an Electrocatalyst for enhanced Electrooxidation of Methanol. *Synth. Met.* **2023**, *293*, 117260.
(32) Chang, J.; Feng, L.; Liu, C.; Xing, W.; Hu, X. Ni 2 P enhances the activity and durability of the Pt anode catalyst in direct methanol fuel cells. *Energy Environ. Sci.* **2014**, *7*, 1628−1632.
(33) Kakaei, K.; Zhiani, M. A new method for manufacturing graphene and electrochemical characteristic of graphene-supported Pt nanoparticles in methanol oxidation. *J. Power Sources* **2013**, *225*, 356−363.
(34) Hong, W.; Wang, J.; Wang, E. Dendritic Au/Pt and Au/PtCu nanowires with enhanced electrocatalytic activity for methanol electrooxidation. *Small* **2014**, *10*, 3262−3265.
(35) Dubouis, N.; Grimaud, A. The hydrogen evolution reaction: from material to interfacial descriptors. *Chem. Sci.* **2019**, *10*, 9165−9181.
(36) Raveendran, A.; Chandran, M.; Dhanusuraman, R. A comprehensive review on the electrochemical parameters and recent material development of electrochemical water splitting electrocatalysts. *RSC Adv.* **2023**, *13*, 3843−3876.
(37) Qin, D.-D.; Tang, Y.; Ma, G.; Qin, L.; Tao, C.-L.; Zhang, X.; Tang, Z. Molecular metal nanoclusters for ORR, HER and OER: Achievements, opportunities and challenges. *Int. J. Hydrogen Energy* **2021**, *46*, 25771−25781.
(38) Jiang, Y.; Guo, Y.; Zhou, Y.; Deng, S.; Hou, L.; Niu, Y.; Jiao, T. Synergism of multicomponent catalysis: one-dimensional Pt-Rh-Pd nanochain catalysts for efficient methanol oxidation. *ACS Omega* **2020**, *5*, 14805−14813.
(39) Zhang, D.; Zhang, X.; Chen, Y.; Wang, C.; Ma, Y.; Dong, H.; Jiang, L.; Meng, Q.; Hu, W. Supercapacitor electrodes with especially high rate capability and cyclability based on a novel Pt nanosphere and cysteine-generated graphene. *Phys. Chem. Chem. Phys.* **2012**, *14*, 10899−10903.
(40) Zhang, D.; Miao, M.; Niu, H.; Wei, Z. Core-spun carbon nanotube yarn supercapacitors for wearable electronic textiles. *ACS Nano* **2014**, *8*, 4571−4579.
(41) Zeng, A.; Bilek, M. M.; McKenzie, D. R.; Lay, P. A.; La Fontaine, A.; Keast, V. J. Correlation between film structures and potential limits for hydrogen and oxygen evolutions at aC: N film electrochemical electrodes. *Carbon* **2008**, *46*, 663−670.
(42) (a) Reier, T.; Oezaslan, M.; Strasser, P. *ACS Catal.* **2012**, *2*, 1765−1772. (b) Lee, Y.; Suntivich, J.; May, K. J.; Perry, E. E.; Shao-Horn, Y. *J. Phys. Chem. Lett.* **2012**, *3*, 399−404.
(43) Tang-Kong, R. Investigation into Stability of Iridium Catalyzed Water Oxidation Photoanodes. Ph.D. Dissertation, Stanford University, 2019.
(44) Shabangoli, Y.; Rahmanifar, M. S.; El-Kady, M. F.; Noori, A.; Mousavi, M. F.; Kaner, R. B. An integrated electrochemical device based on earth-abundant metals for both energy storage and conversion. *Energy Storage Mater.* **2018**, *11*, 282−293.
(45) Ansari, S. A.; Khan, Z.; Ansari, M. O.; Cho, M. H. Earth-abundant stable elemental semiconductor red phosphorus-based hybrids for environmental remediation and energy storage applications. *RSC Adv.* **2016**, *6*, 44616−44629.
(46) Naguib, M.; Mochalin, V. N.; Barsoum, M. W.; Gogotsi, Y. 25th Anniversary Article: MXenes: A New Family of Two-Dimensional Materials. *Adv. Mater.* **2014**, *26*, 992−1005.
(47) Naguib, M.; Kurtoglu, M.; Presser, V.; Lu, J.; Niu, J.; Heon, M.; Hultman, L.; Gogotsi, Y.; Barsoum, M. W. Two-Dimensional Nanocrystals: Two-Dimensional Nanocrystals Produced by Exfoliation of Ti3AlC2 (Adv. Mater. 37/2011). *Adv. Mater.* **2011**, *23*, 4207.
(48) Wu, J.; Wang, Y.; Zhang, Y.; Meng, H.; Xu, Y.; Han, Y.; Wang, Z.; Dong, Y.; Zhang, X. Highly safe and ionothermal synthesis of Ti3C2 MXene with expanded interlayer spacing for enhanced lithium storage. *J. Energy Chem.* **2020**, *47*, 203−209.
(49) Li, K.; Liang, M.; Wang, H.; Wang, X.; Huang, Y.; Coelho, J.; Pinilla, S.; Zhang, Y.; Qi, F.; Nicolosi, V.; et al. 3D MXene architectures for efficient energy storage and conversion. *Adv. Funct. Mater.* **2020**, *30*, 2000842.
(50) Hui, X.; Ge, X.; Zhao, R.; Li, Z.; Yin, L. Interface chemistry on MXene-based materials for enhanced energy storage and conversion performance. *Adv. Funct. Mater.* **2020**, *30*, 2005190.
(51) Kuang, P.; He, M.; Zhu, B.; Yu, J.; Fan, K.; Jaroniec, M. 0D/2D NiS2/V-MXene composite for electrocatalytic H2 evolution. *J. Catal.* **2019**, *375*, 8−20.

https://doi.org/10.1021/acsomega.3c03827
ACS Omega 2023, 8, 34768−34786

(52) Lv, L.; Cai, M.; Jiang, Y.; Wang, Q.; Wang, A.; Chen, J.; Wei, Y.; Cheng, Q.; Sun, S. Priority Occupation of C-Sites by N-Confining P-Implantation in Pyrrodic N-Sites in NCNT@ P, N-Mo2C for Highly Efficient Electrocatalytic Hydrogen Evolution. *Langmuir* **2022**, *38*, 3795−3803.
(53) Jiang, Y.; Sun, T.; Xie, X.; Jiang, W.; Li, J.; Tian, B.; Su, C. Oxygen-Functionalized Ultrathin Ti_3 C_2 T_x MXene for Enhanced Electrocatalytic Hydrogen Evolution. *ChemSusChem* **2019**, *12*, 1368−1373.
(54) Zou, H.; He, B.; Kuang, P.; Yu, J.; Fan, K. Metal−Organic Framework-Derived Nickel−Cobalt Sulfide on Ultrathin Mxene Nanosheets for Electrocatalytic Oxygen Evolution. *Interfaces* **2018**, *10*, 22311−22319.
(55) Ghidiu, M.; Lukatskaya, M. R.; Zhao, M.-Q.; Gogotsi, Y.; Barsoum, M. W. Conductive two-dimensional titanium carbide "clay"with high volumetric capacitance. *Nature* **2014**, *516*, 78−81.
(56) Yu, L.; Hu, L.; Anasori, B.; Liu, Y.-T.; Zhu, Q.; Zhang, P.; Gogotsi, Y.; Xu, B. MXene-bonded activated carbon as a flexible electrode for high-performance supercapacitors. *ACS Energy Lett.* **2018**, *3*, 1597−1603.
(57) Zhang, P.; Zhu, Q.; Guan, Z.; Zhao, Q.; Sun, N.; Xu, B. A Flexible Si@ C Electrode with Excellent Stability Employing an MXene as a Multifunctional Binder for Lithium-Ion Batteries. *ChemSusChem* **2020**, *13*, 1621−1628.
(58) Xu, S.; Wei, G.; Li, J.; Han, W.; Gogotsi, Y. Flexible MXene−graphene electrodes with high volumetric capacitance for integrated co-cathode energy conversion/storage devices. *J. Mater. Chem. A* **2017**, *5*, 17442−17451.
(59) Aierken, Y.; Sevik, C.; Gülseren, O.; Peeters, F. M.; Çakır, D. MXenes/graphene heterostructures for Li battery applications: a first principles study. *J. Mater. Chem. A* **2018**, *6*, 2337−2345.
(60) Karthik, R.; Kumar, J. V.; Chen, S.-M.; Kokulnathan, T.; Chen, T.-W.; Sakthinathan, S.; Chiu, T.-W.; Muthuraj, V. Development of novel 3D flower-like praseodymium molybdate decorated reduced graphene oxide: An efficient and selective electrocatalyst for the detection of acetylcholinesterase inhibitor methyl parathion. *Sens. Actuators, B* **2018**, *270*, 353−361.
(61) Yang, Q.; Xu, Z.; Fang, B.; Huang, T.; Cai, S.; Chen, H.; Liu, Y.; Gopalsamy, K.; Gao, W.; Gao, C. MXene/graphene hybrid fibers for high performance flexible supercapacitors. *J. Mater. Chem. A* **2017**, *5*, 22113−22119.
(62) Lv, Z.; Wang, M.; Liu, D.; Jian, K.; Zhang, R.; Dang, J. Synergetic effect of Ni2P and MXene enhances catalytic activity in the hydrogen evolution reaction. *Inorg. Chem.* **2021**, *60*, 1604−1611.
(63) Liu, J.; Wang, J.; Zhang, B.; Ruan, Y.; Lv, L.; Ji, X.; Xu, K.; Miao, L.; Jiang, J. Hierarchical NiCo2S4@ NiFe LDH heterostructures supported on nickel foam for enhanced overall-water-splitting activity. *ACS Appl. Mater. Interfaces* **2017**, *9*, 15364−15372.
(64) Wang, X.; Luo, D.; Wang, J.; Sun, Z.; Cui, G.; Chen, Y.; Wang, T.; Zheng, L.; Zhao, Y.; Shui, L.; et al. Strain engineering of a MXene/CNT hierarchical porous hollow microsphere electrocatalyst for a high-efficiency lithium polysulfide conversion process. *Angew. Chem., Int. Ed.* **2021**, *60*, 2371−2378.
(65) Lim, K. R. G.; Handoko, A. D.; Johnson, L. R.; Meng, X.; Lin, M.; Subramanian, G. S.; Anasori, B.; Gogotsi, Y.; Vojvodic, A.; Seh, Z. W. 2H-MoS_2 on Mo_2CT_x MXene Nanohybrid for Efficient and Durable Electrocatalytic Hydrogen Evolution. *ACS Nano* **2020**, *14*, 16140−16155.
(66) Jiang, Y.; Li, X.; Yu, S.; Jia, L.; Zhao, X.; Wang, C. Reduced graphene oxide-modified carbon nanotube/polyimide film supported MoS2 nanoparticles for electrocatalytic hydrogen evolution. *Adv. Funct. Mater.* **2015**, *25*, 2693−2700.
(67) Li, F.; Li, J.; Cao, Z.; Lin, X.; Li, X.; Fang, Y.; An, X.; Fu, Y.; Jin, J.; Li, R. MoS2 quantum dot decorated RGO: a designed electrocatalyst with high active site density for the hydrogen evolution reaction. *J. Mater. Chem. A* **2015**, *3*, 21772−21778.
(68) Zhang, Y.; Yang, J.; Dong, Q.; Geng, H.; Zheng, Y.; Liu, Y.; Wang, W.; Li, C. C.; Dong, X. Highly dispersive MoP nanoparticles anchored on reduced graphene oxide nanosheets for an efficient hydrogen evolution reaction electrocatalyst. *ACS Appl. Mater. Interfaces* **2018**, *10*, 26258−26263.
(69) Zhu, Y.; Song, L.; Song, N.; Li, M.; Wang, C.; Lu, X. Bifunctional and efficient CoS2−C@ MoS2 core−shell nanofiber electrocatalyst for water splitting. *ACS Sustain. Chem. Eng.* **2019**, *7*, 2899−2905.
(70) Wang, L.; Wang, J.; Wang, M.; Li, P.; Tong, J.; Yu, F. AgO-decorated multi-dimensional chrysanthemum-like NiCo 2 O 4 mounted on nickel foam as a highly efficient and stable electrocatalyst for the oxygen evolution reaction. *Nanoscale* **2020**, *12*, 7180−7187.
(71) Nie, J.; Hong, M.; Zhang, X.; Huang, J.; Meng, Q.; Du, C.; Chen, J. 3D amorphous NiFe LDH nanosheets electrodeposited on in situ grown NiCoP@ NC on nickel foam for remarkably enhanced OER electrocatalytic performance. *Dalton Trans.* **2020**, *49*, 4896−4903.
(72) Masa, J.; Barwe, S.; Andronescu, C.; Sinev, I.; Ruff, A.; Jayaramulu, K.; Elumeeva, K.; Konkena, B.; Roldan Cuenya, B.; Schuhmann, W. Low overpotential water splitting using cobalt−cobalt phosphide nanoparticles supported on nickel foam. *ACS Energy Lett.* **2016**, *1*, 1192−1198.
(73) Gautam, J.; Liu, Y.; Gu, J.; Ma, Z.; Zha, J.; Dahal, B.; Zhang, L. N.; Chishti, A. N.; Ni, L.; Diao, G.; et al. Fabrication of polyoxometalate anchored zinc cobalt sulfide nanowires as a remarkable bifunctional electrocatalyst for overall water splitting. *Adv. Funct. Mater.* **2021**, *31*, 2106147.
(74) Abdullah, M. I.; Hameed, A.; Zhang, N.; Islam, M. H.; Ma, M.; Pollet, B. G. Ultrasonically surface-activated nickel foam as a highly efficient monolith electrode for the catalytic oxidation of methanol to formate. *ACS Appl. Mater. Interfaces* **2021**, *13*, 30603−30613.
(75) Caffrey, N. M. Effect of mixed surface terminations on the structural and electrochemical properties of two-dimensional Ti 3 C 2 T 2 and V 2 CT 2 MXenes multilayers. *Nanoscale* **2018**, *10*, 13520−13530.
(76) Bai, S.; Yang, M.; Jiang, J.; He, X.; Zou, J.; Xiong, Z.; Liao, G.; Liu, S. Recent advances of MXenes as electrocatalysts for hydrogen evolution reaction. *npj 2D Mater. Appl.* **2021**, *5*, 78.
(77) Zhao, X.; Vashisth, A.; Blivin, J. W.; Tan, Z.; Holta, D. E.; Kotasthane, V.; Shah, S. A.; Habib, T.; Liu, S.; Lutkenhaus, J. L.; Radovic, M.; Green, M. J. pH, nanosheet concentration, and antioxidant affect the oxidation of Ti3C2Tx and Ti2CTx MXene dispersions. *Adv. Mater. Interfaces* **2020**, *7*, 2000845.
(78) Guo, J.; Zhao, Y.; liu, A.; Ma, T. Electrostatic self-assembly of 2D delaminated MXene (Ti3C2) onto Ni foam with superior electrochemical performance for supercapacitor. *Electrochim. Acta* **2019**, *305*, 164−174.
(79) Hussain, S.; Rabani, I.; Vikraman, D.; Feroze, A.; Karuppasamy, K.; Haq, Z. u.; Seo, Y.-S.; Chun, S.-H.; Kim, H.-S.; Jung, J. Hybrid design using carbon nanotubes decorated with Mo2C and W2C nanoparticles for supercapacitors and hydrogen evolution reactions. *ACS Sustain. Chem. Eng.* **2020**, *8*, 12248−12259.
(80) Cao, M.; Wang, F.; Wang, L.; Wu, W.; Lv, W.; Zhu, J. Room temperature oxidation of Ti3C2 MXene for supercapacitor electrodes. *J. Electrochem. Soc.* **2017**, *164*, A3933−A3942.
(81) Fatima, M.; Fatheema, J.; Monir, N. B.; Siddique, A. H.; Khan, B.; Islam, A.; Akinwande, D.; Rizwan, S. Nb-doped MXene with enhanced energy storage capacity and stability. *Front. Chem.* **2020**, *8*, 168.
(82) Ban, F. Y.; Jayabal, S.; Lim, H. N.; Lee, H. W.; Huang, N. M. Synthesis of nitrogen-doped reduced graphene oxide-multiwalled carbon nanotube composite on nickel foam as electrode for high-performance supercapacitor. *Ceram. Int.* **2017**, *43*, 20−27.
(83) Duraivel, M.; Nagappan, S.; Balamuralitharan, B.; Selvam, S.; Karthick, S.; Prabakar, K.; Ha, C.-S.; Kim, H.-J. Superior one-pot synthesis of a doped graphene oxide electrode for a high power density supercapacitor. *New J. Chem.* **2018**, *42*, 11093−11101.
(84) Jia, Z.; Wang, B.; Wang, Y.; Qi, T.; Liu, Y.; Wang, Q. Hierarchical porous nitrogen doped reduced graphene oxide prepared by surface decoration−thermal treatment method as high-activity oxygen reduction reaction catalyst and high-performance supercapacitor electrodes. *RSC Adv.* **2016**, *6*, 49497−49504.
(85) Wen, J.; Jiang, Y.; Yang, Y.; Li, S. Conducting polymer and reduced graphene oxide Langmuir−Blodgett films: a hybrid nano-

https://doi.org/10.1021/acsomega.3c03827
ACS Omega 2023, 8, 34768−34786

structure for high performance electrode applications. *J. Mater. Sci.: Mater. Electron.* **2014**, *25*, 1063−1071.
(86) Cho, S.; Lim, J.; Seo, Y. Flexible Solid Supercapacitors of Novel Nanostructured Electrodes Outperform Most Supercapacitors. *ACS Omega* **2022**, *7*, 37825−37833.
(87) Sharma, S.; Ganguly, A.; Papakonstantinou, P.; Miao, X.; Li, M.; Hutchison, J. L.; Delichatsios, M.; Ukleja, S. Rapid microwave synthesis of CO tolerant reduced graphene oxide-supported platinum electrocatalysts for oxidation of methanol. *J. Phys. Chem. C* **2010**, *114*, 19459−19466.

https://doi.org/10.1021/acsomega.3c03827
ACS Omega 2023, 8, 34768−34786